A Combined Precipitation, Yield Stress and Work Hardening Model for Al-Mg-Si Alloys Incorporating the Effects of Strain Rate and Temperature

By

OLE RUNAR MYHR [1,2], ODD STURE HOPPERSTAD [2] and TORE BØRVIK [2]

1) Hydro Aluminium, Research and Technology Development, N-6601, Sunndalsøra, Norway. Contact E-mail: ole.runar.myhr@hydro.com

2) SIMLab, Centre for Advanced Structural Analysis (CASA), Norwegian University of Science and Technology (NTNU), 7491 Trondheim, Norway

ABSTRACT

In this study, a combined precipitation, yield strength and work hardening model for Al-Mg-Si alloys known as NaMo has been further developed to include the effects of strain rate and temperature on the resulting stress-strain behavior. The modelling is based on a comprehensive experimental database, where thermo-mechanical data for three different Al-Mg-Si alloys are available. In the tests, the temperature was varied between 20 and 350^{o}C with strain rates ranging from 10^{-6} to 750 s^{-1} using ordinary tension tests for low strain rates and a split-Hopkinson tension bar system for high strain rates, respectively. This large span in temperatures and strain rates covers a broad range of industrial relevant problems from creep to impact loading. Based on the experimental data, a procedure for calibrating the different physical parameters of the model has been developed, starting with the simplest case of a stable precipitate structure and small plastic strains, from which basic kinetic data for obstacle limited dislocation glide were extracted. For larger strains, when work hardening becomes significant, the dynamic recovery was linked to the Zener-Hollomon parameter, again using a stable precipitate structure as a basis for calibration. Finally, the complex situation of concurrent work hardening and dynamic evolution of the precipitate structure was analyzed using a stepwise numerical solution algorithm where parameters representing the instantaneous state of the structure were used to calculate the corresponding instantaneous yield strength and work hardening rate. The model was demonstrated to exhibit a high degree of predictive power as documented by a good agreement between predictions and

measurements, and it is deemed well suited for simulations of thermomechanical processing of Al-Mg-Si alloys where plastic deformation is carried out at various strain rates and temperatures.

I. INTRODUCTION

Age hardening Al-Mg-Si aluminum alloys are widely used by the industry since they offer a good combination of properties like strength, ductility, corrosion resistance, formability, and weldability. Precipitation hardening from different types of metastable phases and clusters is the main strengthening contribution in these alloys [1-5], but for many of the properties mentioned above, due consideration must also be given to elements in solid solution as well as dislocation structures that may develop due to different types of forming operations. During thermal processing, the alloys undergo complex structural changes that bring about corresponding changes in the mechanical properties. It is therefore obvious that any model, which intends to capture the effect of the thermomechanical processing on the resulting tensile properties without the use of a vast amount of experimental data, needs an advanced precipitation model as a cornerstone.

During the last decades, several precipitation models have been developed based on the principles outlined in the pioneer works by Langer and Schwarts [6] and Kampmann and Wagner [7,8]. These so-called Kampmann-Wagner (KW) type of models have become increasingly sophisticated and they can incorporate several particle size distributions representing individual phases with various stoichiometry and interface energies as well as different particle shapes [9-13]. Lately they have been integrated with multi-component thermodynamic databases to predict the effect of several alloying elements on the precipitation kinetics [14-18]. These precipitation models are particularly useful when they are coupled with mechanical models based on dislocation mechanics, which allows for predictions of the yield strength and work hardening behavior resulting from a corresponding evolution of the precipitate structure [19-20].

The models by Cheng *et al.* [21] and Poole and Lloyd [22] are well suited for coupling with precipitation models for predictions of the work hardening behavior of age hardening aluminum alloys. They are based on the classical work hardening models by Kocks [23], Mecking and Kocks [24] and Estrin [25,26], but are recast to account for various metallurgical parameters like solute content and number density and size of shearable and non-shearable particles. Even though the models presented by Cheng *et al.* [21] and Poole and Lloyd [22] are useful for work hardening predictions, they are mainly restricted to room temperature deformation where strain rate effects are of less importance for the relevant alloys.

At higher temperatures when strain rate effects become significant, both yield strength and work hardening models must consider kinetic effects. In the present work, a rate equation for plasticity based on obstacle limited dislocation glide is used. This rate equation is based on a prediction of the flow stress at 0 K when the dislocations get no help from thermal fluctuations to overcome barriers they meet in the slip plane. The 0 K flow stress is then adjusted to include strain rate and temperature dependence by considering a dislocation that break through an array of barriers by thermal fluctuations, as explained by Frost and Ashby [27], and Evans and Rawlings [28].

The work hardening model must also consider kinetic effects as the temperature is increased. This has been done in the models by Bergstrøm and Hallén [29] and van den Boogaard and Huétink [30] who introduced the Zener-Hollomon parameter in the expressions for dynamic recovery. These models assume that dislocation climb is the rate controlling recovery mechanism, and that diffusion of vacancies to dislocation cell walls determine the average dislocation climb rate.

An additional complexity when dealing with plastic straining of age-hardening aluminum alloys is that the precipitate structure may change during deformation. Since the precipitate structure evolves by diffusion driven processes, this effect is particularly relevant at relatively high temperatures and low strain rates, which give fast reactions and long exposure times. A realistic prediction of the plastic deformation then requires the use of a numerical solution algorithm. This includes a direct coupling between precipitation, yield strength and work hardening models as has been done in the present work by the use of the NaMo model [31,32]. This model will be briefly described in the following.

II. BRIEF OUTLINE OF THE NAMO MODEL

The symbols and units used throughout the paper are defined in the Appendix. In the past, the relevant structure-property relationships have been captured mathematically in the combined precipitation, yield strength and work hardening model named the nanostructure model (NaMo) [31,32]. The main components of NaMo are shown in Figure 1 together with a description of the transfer of data between the different sub-models, i.e., the precipitation model, the yield strength model and the work hardening model.

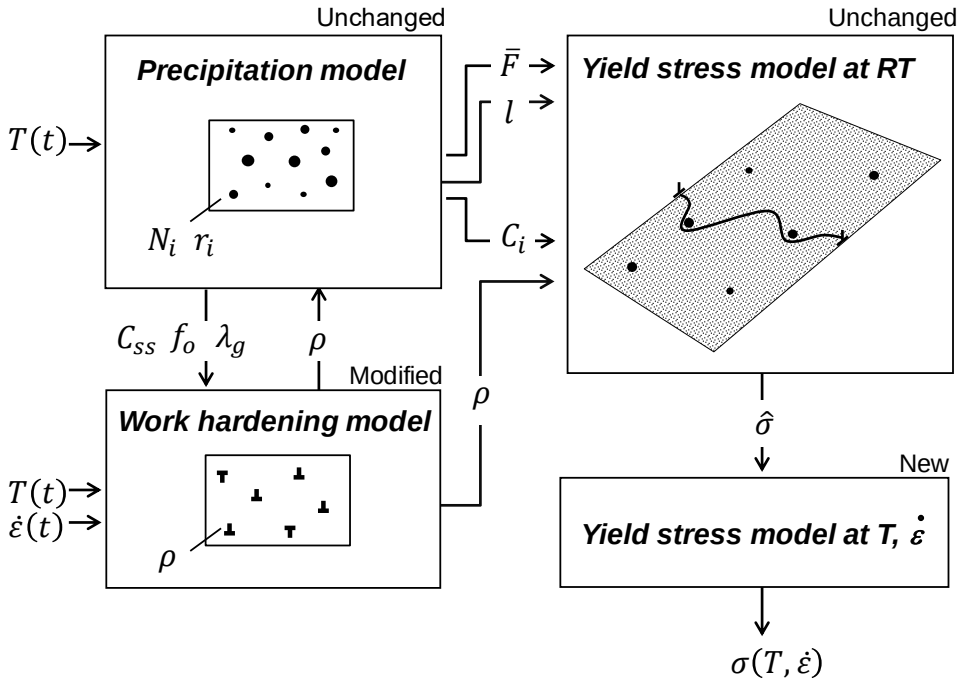

Fig. 1. Coupling of the different sub-models in NaMo, and transfer of data between the sub-models. The symbols used in the figure are explained in the Appendix.

In the present paper, NaMo has been further developed and improved in two ways that makes the model more flexible and relevant for industrial problem solving. Firstly, the model has been extended to include the effect of strain rate and temperature on the yield stress. Secondly, work hardening predictions, which were restricted to room temperature deformations in the previous version of the model, can now account for temperature and strain rate effects through a corresponding extension of the dynamic recovery mechanism.

Details of the underlying assumptions as well as a description of the basic features of the model and the solution algorithm used to capture the evolution of the particle size distributions with time and temperature have been reported elsewhere [20, 32-36]. Hence, only a brief summary of the main constitutive equations is given below.

A. *Precipitation model*

The precipitation model by Myhr and Grong [31,33,34] is based on the Kampmann-Wagner formalism and is the key component of NaMo. The main constituents of the model are the following: (i) nucleation laws, which predict the number of stable nuclei that form at each time step; (ii) rate laws, which calculate either the dissolution or the growth rate of particles within each discrete size class; (iii) a continuity equation, which keeps a record of the amount of solute being tied up as precipitates.

By combining the constituents (i), (ii) and (iii) of the model, and a specially designed solution algorithm based on a control volume formulation [33,34], the particle size distribution (PSD) can be calculated for each time step of the thermomechanical processing history. In the latest version of the model [31], two individual PSDs are included to represent the precipitate structure (i.e., clusters, and metastable β'' and β' particles) as realistic as possible in the simulations.

B. *Yield stress model*

An extract of the outputs from the precipitation model is used to calculate the different contributions to the yield strength σ_y as described by Myhr and co-workers [20,32,35]. The strength contributions are added linearly as follows:

$$\sigma_y = \sigma_i + \sigma_{ss} + \sigma_p + \sigma_d \qquad [1]$$

Here, σ_i denotes the intrinsic yield strength of pure aluminium, which to a reasonable approximation can be set equal to 10 MPa [19]. σ_{ss}, σ_p, and σ_d represent the strength contributions from elements in solid solution, hardening precipitates and dislocations, respectively.

Note that the justification of using Eq. [1] relies solely on the fact that it has proved to work well in many other situations [20,31,32, 34-38], because the assumption of linear additive strength contributions is just one of several possible options to choose from when calculating σ_y [39-41].

144 *1. Solid solution hardening*

145 In NaMo, the contribution from elements in solid solution to the yield stress,
146 i.e., σ_{ss} in Eq. [1], is calculated as follows [20, 31]:

$$\sigma_{ss} = \sum_i k_i \, C_i^{2/3} \qquad [2]$$

147 where C_i is the concentration of a specific element in solid solution and k_i is the
148 corresponding scaling factor for the relevant elements with values given in Reference
149 31. For the elements Mg and Si, the solid solution concentrations, i.e., C_{Mg} and C_{Si},
150 vary during a heat treatment depending on the volume fraction of clusters and
151 metastable particles. An increase of these volume fractions is followed by a
152 corresponding decrease of C_{Mg} and C_{Si} since elements are gradually removed from the
153 matrix when clusters and metastable particles are formed. This is accounted for by the
154 continuity equation, which is an integrated part of the precipitation model.

155 *2. Precipitation hardening*

156 The strength contribution from particles is calculated using the following
157 relationship [19,20]:

$$\sigma_p = \frac{M\bar{F}}{bl} \qquad [3]$$

158 Here, M is the Taylor factor, b is the magnitude of the Burgers vector, $\bar{F}$ is the mean
159 obstacle strength, and l is the effective particle spacing in the slip plane along the
160 bending dislocation. Both $\bar{F}$ and l are explicitly defined by the particle size distribution
161 as explained in References 20 and 35, and Eq. [3] therefore represents a direct coupling
162 between the precipitation model and the yield strength model as illustrated in Figure 1.

163 Since NaMo contains two individual particle size distributions, i.e., one for
164 clusters, and one for metastable β'' and β' particles, two strength contributions are
165 calculated, namely σ_{p1} and σ_{p2}, representing each of these distributions. The overall
166 hardening from particles is given by the following expression [31]:

$$\sigma_p = \sqrt{\sigma_{p1}^2 + \sigma_{p2}^2} \qquad [4]$$

In this equation, σ_{p1} and σ_{p2} are both calculated from Eq. [3] using individual values for $\bar{F}$ and l extracted from each of the two particle size distributions as described in more details in Reference 31.

The reason why the strength contributions σ_{p1} and σ_{p2} are added according to Eq. [4] is because the obstacles responsible for these two contributions are comparable with respect to strength. When this is the case, Eq. [4] is usually recognized to be a more realistic way of adding strength contributions than a simple linear summation [40].

C. *Work hardening*

The final term in Eq. [1], σ_d, represents the contribution from dislocations to the yield stress as calculated by the work hardening model. The total dislocation density ρ is assumed to be the sum of statistically stored dislocations ρ_s and geometrically necessary dislocations ρ_g, and their contribution to the yield stress, σ_d, is given by the following equation [42]:

$$\sigma_d = \alpha M \mu b \sqrt{\rho_s + \rho_g} \qquad [5]$$

Here, α is a constant with a value close to 0.3, and μ is the shear modulus for which the temperature dependence is accounted for through the following empirical expression [43]:

$$\mu = \mu_0 \left(1 - \frac{T}{T_m} \exp\left(\theta_g \left(1 - \frac{T_m}{T}\right)\right)\right) \qquad [6]$$

Here, μ_0 is the shear modulus at 0 K, T_m is the melting temperature of the material, and θ_g is a material constant given in Table I.

Note that ρ_s and ρ_g not only affect the flow stress directly through Eq. [5], but also affect the precipitation structure that forms since nucleation of metastable β' particles along dislocation lines takes place to an increasing extent during ageing when the dislocation density increases [44, 45]. In NaMo, this gradual transition from matrix nucleation of β'' particles to nucleation of β' particles at dislocations with increasing ρ_s is accounted for through the back-coupling from the work hardening model to the precipitation model as illustrated in Figure 1 [31].

Evolution equation for ρ_s

The Kocks-Mecking relationship gives the evolution of the statistically stored dislocations as follows [23, 24]:

$$\frac{d\rho_s}{d\varepsilon_p} = k_1\sqrt{\rho_s} - k_2\rho_s \qquad [7]$$

Here, k_1 is a constant being characteristic for the material under consideration, whereas the parameter k_2 determines the rate of the dynamic recovery during plastic deformation, and depends on the solute content of the alloy.

Since dynamic recovery depends on temperature and strain rate, k_2 may be correlated with the Zener-Hollomon parameter according to the model by Bergstrøm and Hallén [29]. This model assumes that dislocation climb is the dominant dynamic recovery mechanism, and that diffusion of vacancies to dislocation cell walls is the rate controlling reaction determining the average dislocation climb rate. In the present work, the following dynamic recovery expression, which is based on the Bergstrøm model, is used [30]:

$$k_2 = k_2^*\left[1 + \left(\frac{Z_s}{Z}\right)^m\right] \qquad [8]$$

where k_2^*, m and Z_s are constants. The Zener-Hollomon parameter Z is given as:

$$Z = \dot{\varepsilon}_p \exp\left(\frac{Q_v}{RT}\right) \qquad [9]$$

where R and T are the universal gas constant (8.314 kJ/mol) and the absolute temperature in Kelvin, respectively, while Q_v is the activation energy for vacancy diffusion which is close to 68.8 kJ/mol for aluminum [46].

The present version of NaMo contains a work hardening model for Al-Mg-Si alloys that is valid for plastic straining at room temperature, where the Zener-Hollomon parameter is high, i.e., $Z \gg Z_s$, and thus $k_2 \approx k_2^*$. This model accounts for the effect of elements in solid solution on the dynamic recovery in a semi-empirical manner.

According to this model, the dynamic recovery at room temperature, corresponding to k_2^*, can be expressed as follows [32]:

$$k_2^* = k_1 \frac{\alpha M \mu b}{k_3 (C_{ss})^{\frac{3}{4}}} \quad [10]$$

Here, k_3 is a parameter governing the influence of solutes on k_2^*, and C_{ss} is an effective solid solution concentration, which includes a weighted overall effect of Mg and Si in solid solution on the dynamic recovery rate based on experiments [32]. Since C_{ss} changes continuously during a heat treatment as predicted by the precipitation model of NaMo, it is evident that k_2^* changes correspondingly according to Eq. [10].

By combining Eqs. [8] and [10] we get:

$$k_2 = k_1 \frac{\alpha M \mu b}{k_3 (C_{ss})^{\frac{3}{4}}} \left[1 + \left(\frac{Z_s}{Z} \right)^m \right] \quad [11]$$

It is now convenient to introduce k_2^0 corresponding to k_2 for a reference alloy at 0 K. The reference alloy has an effective solid solution concentration C_{ss}^r and a Zener-Hollomon parameter and shear modulus equal to Z_0 and μ_0, respectively, where index 0 means 0 K. It follows from Eq. [9], that $Z_0 = \infty$. If it is assumed that the Taylor factor for the reference material is equal to the one for the actual alloy, i.e., $M_r = M$, Eq. [11] can be simplified as follows:

$$k_2 = k_2^0 \left(\frac{\mu}{\mu_0} \right) \left(\frac{C_{ss}^r}{C_{ss}} \right)^{\frac{3}{4}} \left[1 + \left(\frac{Z_s}{Z} \right)^m \right] \quad [12]$$

Here, C_{ss}^r is a reference concentration used for scaling, which has been set equal to 1.0 wt% in the present work. The selected values for k_2^0 and Z_s are given in Table I, and the calibration of the parameters is explained in Section IV.

Evolution equation for ρ_g

According to Ashby [47], the effectiveness of particles, grain or phase boundaries in causing dislocations to be stored during plastic deformation is conveniently described by the geometric slip distance λ_g. For alloys containing non-shearable particles, this storage of dislocations is necessary to obtain compatibility of the two phases during

deformation. The present type of alloys may contain a significant volume fraction of particles with a radius larger than the critical radius for the transition between shearing and bypassing of particles by dislocations, and these particles contribute to the storing of geometrically necessary dislocations. By applying the expressions derived for the geometric slip distance of a homogeneous distribution of equiaxed particles [47], the following expression for λ_g for a particle size distribution can be derived [32,34]:

$$\lambda_g = \left(8 \sum_{r=r_c}^{r=\infty} r_i^2 N_i \right)^{-1} \quad [13]$$

Here, N_i is the number of particles per unit volume within the size class r_i, and r_c is the critical radius for the transition from shearing to bypassing of the particles by dislocations.

Similarly as for statistically stored dislocations, the evolution law for geometrically necessary dislocations can be expressed by two terms, i.e., one for storing of dislocations and one for dynamic recovery. The evolution law for ρ_g given in Reference 32 can then be recast in the following form:

$$\frac{d\rho_g}{d\varepsilon_p} = \frac{k_{1g}}{\lambda_g} - k_{2g}\rho_g \quad [14]$$

where k_{1g} and k_{2g} are material constants. By introducing a similar expression for the dynamic recovery as was used for statistically stored dislocations in Eq. [8], the effect of strain rate and temperature can be included in k_{2g} as follows:

$$k_{2g} = k_{2g}^0 \left(\frac{f_o}{f_o^r} \right) \left[1 + \left(\frac{Z_g}{Z} \right)^m \right] \quad [15]$$

Here, k_{2g}^0 is the dynamic recovery constant for the reference alloy, for which $Z \gg Z_g$ and $f_o = f_o^r$. In Eq. [15], it is assumed that k_{2g} is proportional to the volume fraction of non-shearable particles f_o, which can be derived from the expressions given in Reference 33. The values used for k_{2g}^0, f_o^r, and Z_g are given in Table I.

The net contribution from dislocation hardening σ_d

In the special case when the precipitate structure remains constant during plastic deformation at the same time as the plastic straining is carried out using constant strain rate and temperature, the net contribution from dislocation hardening σ_d can be calculated by a simple analytical equation that is derived by integrating the dislocation densities ρ_s and ρ_g from Eqs. [7] and [14], respectively, and substituting the values into Eq. [5]. This gives the following expression:

$$\sigma_d = \alpha M \mu b \sqrt{\left(\frac{k_1}{k_2}\right)^2 \left(1 - \exp\left(-\frac{k_2 \varepsilon_p}{2}\right)\right)^2 + \left(\frac{k_{1g}}{\lambda_g k_{2g}}\right)\left(1 - \exp\left(-k_{2g}\varepsilon_p\right)\right)} \qquad [16]$$

In this expression, the effects of temperature and strain rate are included in the dynamic recovery constants k_2 and k_{2g}, which both depend on temperature and strain rate via the Zener-Hollomon parameter Z, see Eqs. [12] and [15], respectively.

It is important to note that Eq. [16] cannot be used in the general situation when the precipitate structure evolves during the plastic deformation, or when the strain rate or the temperature is not constant. In such situations, the only way of calculating σ_d is numerically with a stepwise increase in time, and where incremental changes in the relevant solute and precipitate parameters (i.e., C_{ss}, f_o and λ_g) are transferred to the work hardening model for each time step. As shown in Fig. 1, there must also be a transfer of data in the opposite direction for each time step, i.e., from the work hardening model to the precipitation model, since the nucleation laws embedded in the precipitation model depend on the dislocation density, as described in Reference 31.

D. *Framework for modelling the relationship between stress, strain rate, and temperature*

The applications of the previously developed yield stress model of NaMo [20,31,35] have been restricted to calculations of the flow stress σ_y at room temperature without considering the effect of strain rate. The assumption that strain rate effects can be neglected at room temperature has been confirmed by measurements conducted for these types of alloys [48,49].

Obstacle limited dislocation glide

In order to include the effects of temperature and strain rate on the yield strength, a model based on obstacle limited dislocation glide has been chosen. This model is derived on the basis of the Orowan equation which describes the relationship between the average speed of the mobile dislocations and the strain rate, and introduces the Gibbs free energy of cutting or bypassing of barriers as a function of the applied stress [27, 50]. The resulting flow stress σ can then be expressed as follows [27,50]:

$$\sigma = \hat{\sigma}\frac{\mu(T)}{\mu_0}\left\{1 - \left[\frac{RT}{\Delta G}\ln\left(\frac{\dot{\varepsilon_0}}{\dot{\varepsilon}_p}\right)\right]^{1/q}\right\}^{1/p} \quad [17]$$

Here, $\hat{\sigma}$ can be considered as the yield stress at 0 K, i.e., when the barriers are overcome in the absence of any thermal activation. ΔG is the total free energy corresponding to the activation energy required to overcome the obstacle without aid from external stresses. The constants p and q depend on the spatial distribution and shape of the obstacles [27, 50]. Their values may vary between the following boundaries [27], i.e., $0 \leq p \leq 1$ and $1 \leq q \leq 2$, but the influence of their numerical value is relatively small for sufficiently large ΔG-values [27]. In the present work, p and q are assumed to be equal to 1 as a reasonable approximation which has previously been used for similar types of aluminum alloys [51].

It follows from the derivation of Eq. [17] that the reference strain rate $\dot{\varepsilon}_0$ is proportional to the mobile dislocation density. As pointed out in Reference 27, $\dot{\varepsilon}_0$ can to a reasonable degree of accuracy be considered as a constant for sufficiently large ΔG values. As will be shown later, ΔG is indeed relatively large for the present alloys, which justifies the use of a constant reference strain rate $\dot{\varepsilon}_0$ for which a numerical value of 10^6 s^{-1} has been adopted [27] as given in Table II.

Relationship between room-temperature yield stress and yield stress at 0 K

The next step is to couple the previously developed room-temperature yield stress model to the new yield stress model that includes the effect of temperature and strain rate. This can readily be done by inserting the room temperature in Kelvin, $T_r = 298$ K, and the representative strain rate $\dot{\varepsilon}_r = 10^{-4}\mathrm{s}^{-1}$ that was used when calibrating

315 the RT yield stress model into Eq. [17]. If σ_y denotes the resulting flow stress at room
316 temperature, Eq. [17] gives:

$$\sigma_y = \hat{\sigma}\frac{\mu(T_r)}{\mu_0}\left\{1 - \left[\frac{RT_r}{\Delta G}\ln\left(\frac{\dot{\varepsilon}_0}{\dot{\varepsilon}_r}\right)\right]^{1/q}\right\}^{1/p} \quad [18]$$

317 which can be expressed as:

$$\sigma_y = c_1\hat{\sigma} \quad [19]$$

318 Thus, the constant c_1 is given as follows:

$$c_1 = \frac{\mu(T_r)}{\mu_0}\left\{1 - \left[\frac{RT_r}{\Delta G}\ln\left(\frac{\dot{\varepsilon}_0}{\dot{\varepsilon}_r}\right)\right]^{1/q}\right\}^{1/p} \quad [20]$$

319 By inserting the calibrated ΔG value from Table II, Eq. [20] gives $c_1 = 0.83$. Even
320 though the value of the representative strain rate $\dot{\varepsilon}_r$ used to estimate c_1 is not exact, as
321 different strain rates were used in the previous calibration of the RT yield stress model,
322 this is not critical for the resulting value of c_1 because $\dot{\varepsilon}_r$ enters a logarithmic term in
323 Eq. [20].

324 When an estimated value of c_1 has been established, Eq. [19] can be used to
325 convert the yield stress at room temperature, σ_y, to a corresponding yield stress at 0 K,
326 $\hat{\sigma}$, and then this value can be substituted into Eq. [17] to get the temperature and strain
327 rate dependent flow stress σ, as illustrated in Figure 1.

328

329 **III. EXPERIMENTAL**

330 The experiments referred to in the present investigation were conducted on three
331 different alloys with chemical composition as shown in Table III. Each of these alloys
332 has been processed, heat treated, and tested differently to obtain a broad range of
333 precipitate structures, testing temperatures and strain rates, as summarized in Table IV.
334 The alloys were delivered by Hydro Aluminium, but in different conditions as
335 explained in the following.

336

337

338 A. *Processing and testing of alloys*

339 *Alloy A1*

340 A detailed description of the processing, heat treatment and testing of alloy A1
341 is given in References 49 and 51-53. Briefly, the alloy was delivered in the cast and
342 homogenized condition, from which cylindrical tensile specimens with 3 mm diameter
343 in the minimum cross-section were prepared along the axis of the cylindrical billet. The
344 alloy was tested in this condition to avoid anisotropy, which inevitably will result from
345 an extrusion process. Note that the initial condition of alloy A1 is called W in the present
346 work, even though this may not be strictly correct according to the Aluminium
347 Association designation system, since the alloy was not subjected to any forming
348 operations prior to the testing.

349 The experimental program involved tension tests at different strain rates and
350 temperatures. The strain rate varied between 0.01 and 750 s^{-1}, and the temperature
351 between 20 to 350^{o}C. The tests were carried out after about 6 months storing at room
352 temperature. The tests at low and moderate strain rates, i.e., from 0.01 to 1 s^{-1}, were
353 carried out in a Zwick-Roell testing machine, while the tests at higher strain rates were
354 carried out using a split-Hopkinson tension bar system [52,53].

355 *Alloy A2*

356 References 48 and 54 give an outline of how alloy A2 was processed, heat-
357 treated and tested. Extruded profiles with a thickness of 1.8 mm were cut into dogbone-
358 shaped test specimens with a 30 mm straight and a 8 mm wide central section. The
359 length direction of the samples was parallel to the extrusion direction. The samples were
360 then solution heat-treated, water quenched, and artificially aged to peak strength (T6)
361 condition by ageing for 9 hours at 170^{o}C. The elongation of a 10 mm long section was
362 measured by an extensometer during the Gleeble tests, which were carried out using
363 the sample geometry described above, and with a thermocouple spot welded to the mid-
364 position in order to control that the temperature follows the pre-set thermal program.

365 The Gleeble testing of each sample was carried out in two successive
366 thermomechanical cycles in order to compare the material response of the alloy in two
367 different initial conditions, i.e., artificially aged to peak strength (T6), and as solution
368 heat treated (W), respectively. In the first cycle, the T6-samples were heated to the test
369 temperature with a heating rate of about 30^{o}C/s. A strain rate of 10^{-3} s^{-1} was imposed to

the sample as soon as the prescribed test temperature was reached. After about 6% plastic deformation, the straining was interrupted and a separate solution heat treatment at 540^{o}C for 10 seconds holding time was enforced to the sample. The heating and cooling rates used for this solution heat treatment cycle were approximately 30 and 50 ^{o}C/s, respectively. During this thermal cycle, the samples were free to move in the grips to avoid deformation due to thermal expansion and contraction.

The intention of imposing this intermediate heating cycle was to obtain a full solution heat treatment of the alloy and to keep Mg and Si in solution by a rapid cooling. At the same time, the dislocation hardening contribution was intended reset to a low level by recovery and recrystallisation reactions, which are very fast at 540^{o}C. In this way, the temper of the alloy can be considered to correspond closely to the as-solution heat-treated W-condition at the start of the second thermomechanical cycle.

The second thermomechanical cycle was then carried out for the samples in the initial W-condition similarly as the one for the initial T6-condition, i.e., by imposing a constant strain rate to the Gleeble sample as soon as the prescribed temperature was reached.

Alloy A3

Cast aluminum billets were homogenized at 575^{o}C for about 2 hours and extruded to flat profiles with cross section 150 mm × 5 mm followed by water quenching. Dogbone-shaped test samples were prepared with the tensile axis parallel to the extrusion direction, and with a 30 mm straight central section with 6 mm width in the transverse direction and 5 mm thickness in the direction normal to the surface of the profile corresponding to the profile thickness. After preparation, the samples were solution heat treated at 540^{o}C for 30 minutes followed by water quenching prior to artificial ageing at 160^{o}C for 10 hours to achieve the desired maximum strength corresponding to the T6-condition.

Gleeble experiments were carried out similarly as for Alloy 2 described above, with testing of the material in the initial T6-condition first, followed by an intermediate solution heat treatment at 540^{o}C for 10 seconds to obtain W-temper condition prior to the second testing cycle at different temperatures. Three different strain rates were used in the experiments, namely 10^{-5}, 10^{-4} and 10^{-3} s^{-1}.

IV. THE STABILITY OF THE PRECIPITATE STRUCTURE

The precipitation model is a key component of NaMo since the outputs from this model are inputs to the integrated yield strength and work hardening models as described in Figure 1. This allows the full stress-strain curve to be calculated for different alloy compositions and thermal treatments. It is obvious that calculations of these mechanical properties rely on accurate predictions by the precipitation model. The model has been developed to a stage where it seems to capture many of the complex reactions that are associated with thermomechanical processing of Al-Mg-Si alloys, and it has previously been validated by comparison with experimental microstructure data obtained from transmission electron microscope (TEM) examinations covering a broad range of experimental conditions. The TEM validations include the effect of various ageing and reheating cycles for different alloy compositions [20], and the effect of rapid heating and cooling cycles as experienced in the heat-affected zone during welding [35].

A. *Comparison of measured and predicted precipitate structure parameters*

An example of the predictive capability of the precipitation model is shown in Figure 2, where TEM bright field images are presented after various heat treatments of an Al-Mg-Si alloy containing 0.82wt% Si and 0.55wt% Mg. A detailed description of the alloy and the processing conditions is given in Reference 35. Figure 2(a) shows TEM bright field images after 5 hours at 185^{o}C corresponding to the T6 condition, and after subsequent heating to 315^{o}C (Figure 2(b)) and 390^{o}C (Figure 2(c)), respectively, with 10 seconds holding time for both temperatures. In Figure 2(d), precipitate parameters obtained from a statistical analysis of the TEM images are compared with corresponding parameters calculated by the precipitation model in NaMo. From this figure, it is evident that the particle number density drops by about two orders of magnitudes when the T6 heat-treated material is reheated to 390^{o}C. At the same time, there is a coarsening of the precipitate structure as the mean particle size in terms of the equivalent spherical radius of the particles, increases from about 4nm to 17nm. As can be seen, the overall agreement between predictions by the precipitation model and measurements is good for all the heat treatments presented in the figure.

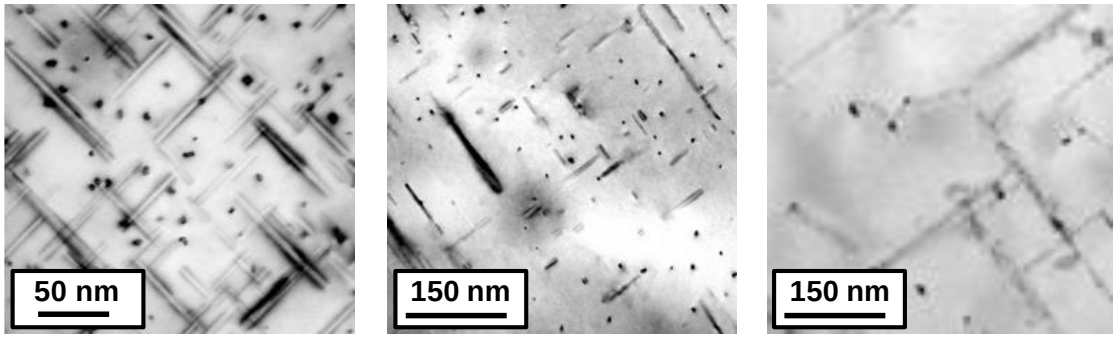

(a) (b) (c)

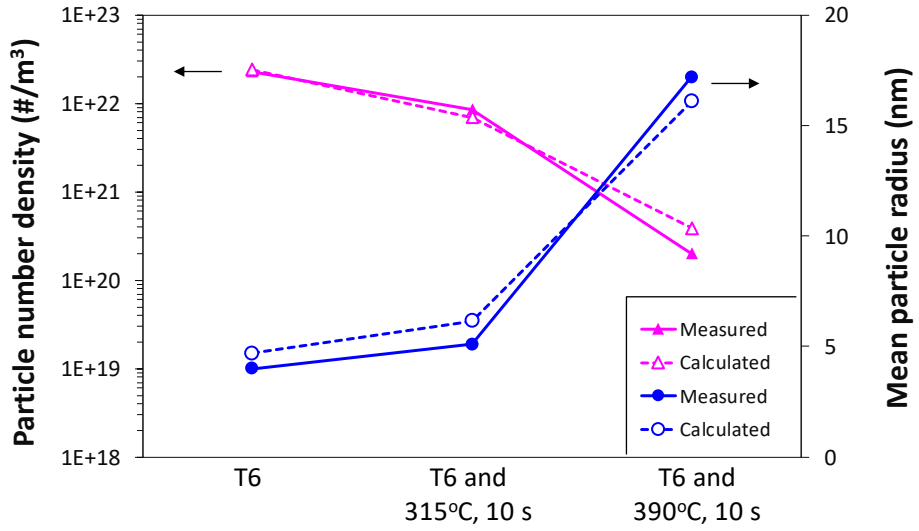

(d)

Fig. 2. Example of the predictive capability of the precipitation model in NaMo. Figures (a), (b) and (c) show TEM bright field images of microstructures observed in the <100> Al zone axis orientation after artificial ageing and Gleeble simulation [35]. (a) Needle-shaped β'' precipitates which form after a T6 heat treatment corresponding to solution heat treatment at 530°C for 30 minutes followed by water quenching prior to artificial ageing at 185°C for 5 hours. (b) Mixture of coarse rod-shaped β' particles and fine needle-shaped β'' precipitates which form after subsequent thermal cycling to $T_p = 315℃$ (10 seconds holding time). (c) Coarse rod-shaped β' particles which form after subsequent thermal cycling to $T_p = 390℃$ (10 seconds holding time). (d) Comparison between predictions by the precipitation model and measurements of the particle number density (left-hand axis) and the mean particle radius (right-hand axis).

B. *Boundaries between stable and non-stable precipitate structures*

As explained in the previous sections, the stability of the precipitate structure determines which solution that should be used to calculate the stress-strain response during thermomechanical processing. A stable precipitate structure allows for the use of simple analytical solutions, while a non-stable precipitate structure requires the use of more complex numerical solution algorithms with continuous updates of the precipitate structure as input to the yield strength and work hardening models for each timestep of the simulation like the one outlined in Figure 1.

The selection of the most appropriate solution algorithm therefore requires that the combinations of temperature and time where the precipitates remain essentially stable during a thermomechanical process are known. This depends on the state of the precipitate structure at the start of the process because the rate at which a precipitate structure decomposes and transforms by diffusion driven reactions depends on the initial solid solution level as well as the particle size distribution of the different metastable phases.

In order to predict the boundaries between stable and non-stable precipitate structures, a systematic series of simulations using the complete NaMo model was undertaken. In these simulations, the precipitate structure at the start of an assumed tensile test was first simulated for two different ageing heat treatments corresponding to the solution heat treated (W) and the peak aged (T6) conditions, respectively. In all simulations, the alloy composition was fixed to the one for alloy A2 in Table III. From each of these two starting conditions, isothermal heat treatments at different temperatures were run by NaMo, and the results were subsequently analyzed in order to detect when the precipitate structure started to deviate significantly from the initial structure at the start of the isothermal heat treatment. This deviation in precipitate structure will be reflected in a corresponding change in the flow stress as predicted by the yield stress model of NaMo, and the boundary between a stable and non-stable structure was defined as the temperature-time combination that gives a 5% deviation (positive or negative) in the yield stress compared with the initial value.

Figure 3 shows the calculated boundaries between stable and non-stable precipitate structures based on these simulations. To the left of the boundaries, the precipitate structures are essentially unchanged compared with the starting condition,

while they have changed compared with the starting conditions at the right-hand side of the boundaries. It is evident from the figure that the shape and location of the two boundaries are significantly affected by the initial condition. Hence, for the T6-condition, the structural changes occur fast at high temperatures. This is because this structure contains metastable particles after the T6-heat treatment, and these particles start to dissolve when the temperature is increased. For instance, at 300°C, it takes about 0.1 seconds before a 5% deviation is observed in the simulations since the smaller particles of the distributions dissolve very fast at this temperature. For the W-temper, the corresponding time at 300°C is about 15 seconds, because this structure contains only elements in solid solution from the start. The decomposition of the solid solution requires that particles form by nucleation, which is a slower process at this temperature than the corresponding dissolution reaction, which is the dominant reaction for the T6-condition.

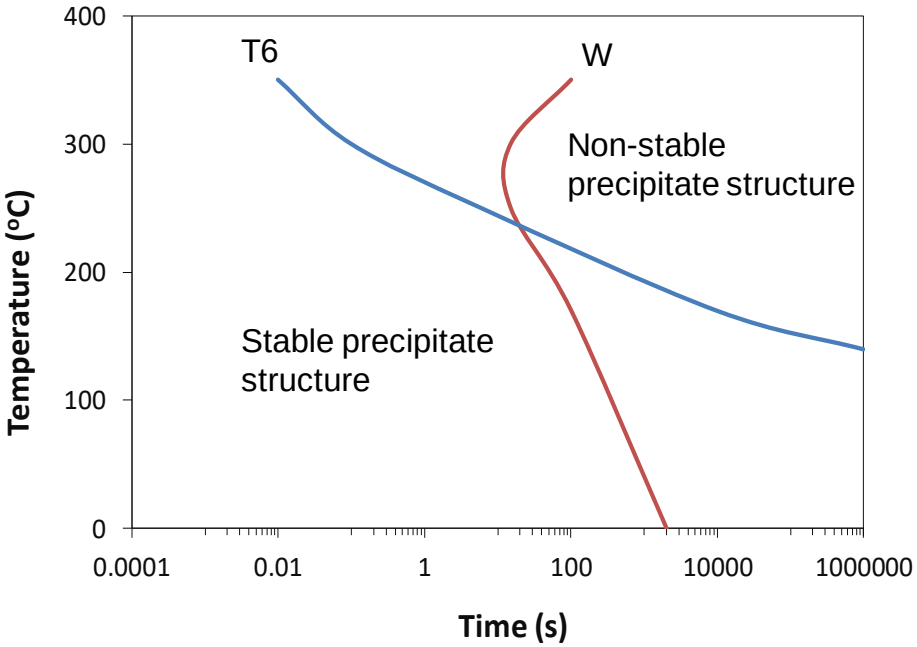

Fig. 3. Calculated boundaries between stable and non-stable precipitate structures for two different initial conditions, i.e., as-solution heat treated (W) and peak aged (T6).

At 240°C, the two curves intercept, and below this temperature, the W-condition is the less stable of the two conditions in the sense that it takes shorter time to reach a 5% deviation in properties compared with the T6-condition. Again, this is due to the

difference between the rate controlling reactions for the two conditions. At relatively low temperatures, nucleation is faster than the dominating reactions for the existing particle size distributions in the T6-condition, which are dissolution and growth reactions.

In Figures 4(a) and 4(b), the experiments conducted for each of the three alloys A1, A2 and A3 are collected with respect to applied temperatures and holding times for the initial conditions W and T6, respectively. It is evident that the precipitate structures are essentially stable for most of the tests, as the symbols are mainly located at the left-hand side of the two boundaries. For alloy A1, some of the symbols in Figure 4(a) are located to the right of the boundary, indicating a non-stable structure. It is, however, more likely that also these symbols represent stable structures, since alloy A1 was not given a separate solution heat treatment after homogenization. This means that the vacancy and solid solution concentrations are probably lower than what have been assumed in the simulations, and the rates of the precipitation reactions are therefore likely to be overestimated. Hence, only one symbol in Figure 4(a) and three symbols in Figure 4(b) are clearly on the right-hand side of the boundaries indicating a non-stable precipitate structure, and these will be discussed later in Section V.

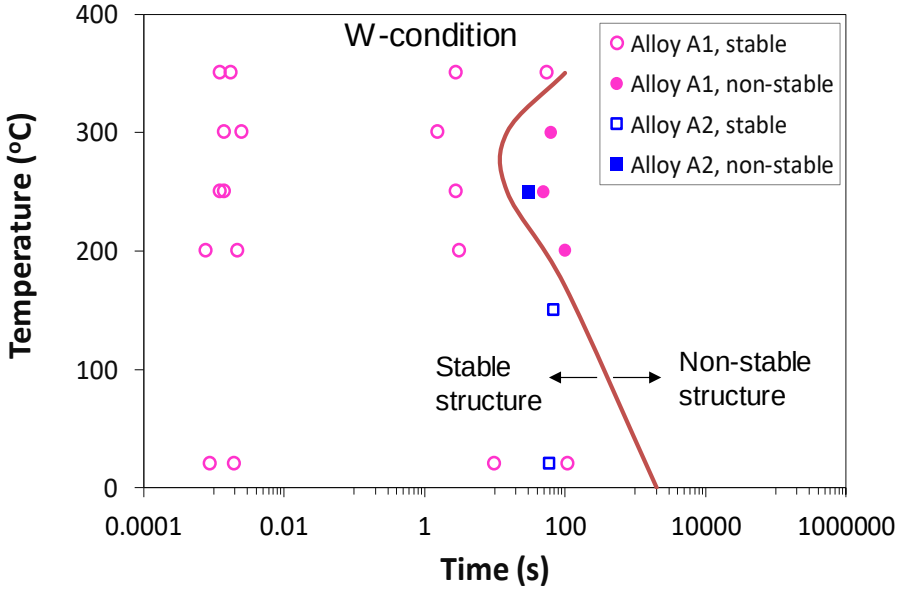

(a)

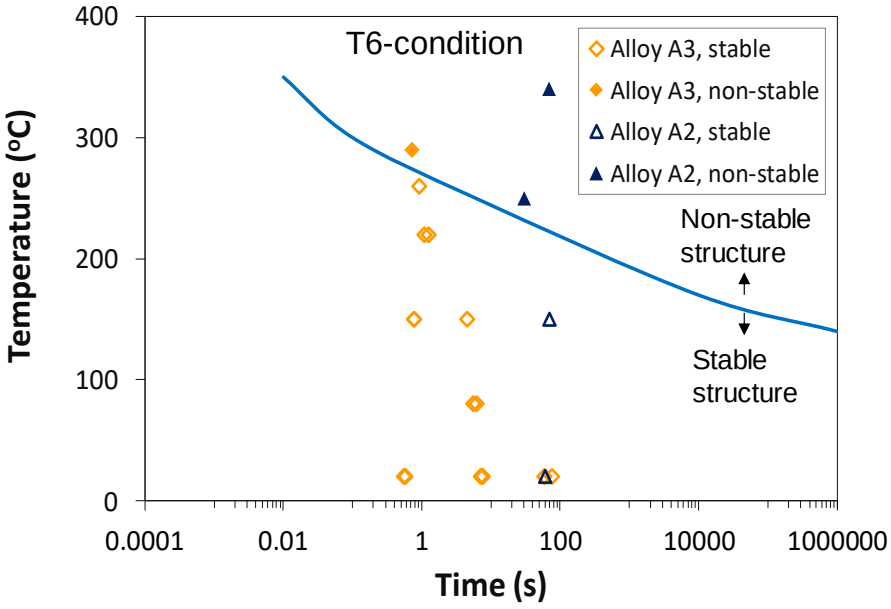

(b)

Fig. 4. Overview of applied temperature and holding time for all tests. The location of the symbols in the diagram relative to the superimposed boundaries indicates whether they are performed with a stable (open symbols) or non-stable (filled symbols) precipitate structure. (a) Initially as-solution heat-treated (W) condition. (b) Initially peak aged (T6) condition.

Even though the selected alloy composition used to predict the boundaries in Figure 3 corresponds to alloy A2, similar simulations carried out for various Al-Mg-Si alloys indicate that the boundaries are relatively insensitive to composition and they can therefore be used to a first approximation also for other alloys like A1 and A3 in the present investigation. Another simplification used to estimate the boundaries in Figures 3 and 4 is that no evolution of dislocation structures was considered in the simulations. Accordingly, the back-coupling from the work hardening model to the precipitation model, shown in Figure 1, is not accounted for in Figure 3. This is however deemed to have minor influence on the resulting location of the boundaries for the T6-condition where a precipitate structure exists at the start, but it can have some influence

on the predicted boundary for the W-condition, for which precipitation of β' particles on dislocations that form during the plastic deformation is possible.

V. CALIBRATION AND VALIDATION OF MODEL

A. *Stable precipitate structure*

No work hardening

The first step is to calibrate the model for small plastic strains when the work hardening can be ignored. This reduces the number of adjustable parameters since $\hat{\sigma}$ can be assumed to be constant if the dislocation density does not increase significantly by work hardening and the time for completing the tensile test is short enough to avoid a significant evolution of the precipitate structure.

The activation energy ΔG was estimated based on measured data for small plastic strains by rearranging Eq. [17], and substitute σ_y for $\hat{\sigma}$ from Eq. [19], which gives:

$$\frac{1}{RT}\left(c_1 \frac{\sigma}{\sigma_y}\frac{\mu_0}{\mu(T)} - 1\right) = \frac{1}{\Delta G}\left(\ln \dot{\varepsilon}_p - \ln \dot{\varepsilon}_0\right) \qquad [21]$$

From Eq. [21], it follows that a plot of the left-hand expression versus $\ln \dot{\varepsilon}_p$ gives a straight line with slope $1/\Delta G$. This requires that the constant c_1 is known. Since this constant depends on ΔG according to Eq. [21], an iteration procedure is required to determine the value of this constant. A reasonable value of ΔG must first be guessed upon as a basis for estimating an initial c_1-value. Then a new plot of Eq. [21] can be made from which an updated ΔG-value is obtained and so forth. This procedure was used for the experimental data available for alloy A1, and gave c_1 equal to 0.83. This has been used for the plots in Figure 5. The symbols represent tensile yield stresses recorded at a plastic strain of 0.01, which is assumed sufficiently small to justify ignoring work hardening in the calculations.

The experimental data plotted in Figure 5 do not show any clear evidence of one common ΔG-value that represents all the temperatures, since the slope of the curves varies. Furthermore, the fact that the curves are displaced along the vertical direction may indicate that the reference strain rate $\dot{\varepsilon}_0$ is not constant in these tests, but varies

with temperature. However, to keep the model as simple as possible, these parameters were kept constant for all simulations in the present work. The simulation results presented in the following sections indicate that this is a reasonable approximation.

From the slope of each line in Figure 5, the corresponding ΔG-values were estimated to vary between a lower value of approximately 200 kJ/mol for the 350°C line, to an upper value of about 300 kJ/mol representing the average slope of the other lines in the diagram. These ΔG-values can alternatively be expressed as 0.53 and 0.80 $\mu_0 b^3$, respectively, which agree well with literature data for medium strength obstacles, for which ΔG typically varies between 0.2 and 1.0 $\mu_0 b^3$ according to Frost and Ashby [27]. In the present modelling, the ΔG-value of 300 kJ/mol was chosen since this value gave a better overall fit between modelling results and measurements than a lower ΔG-value.

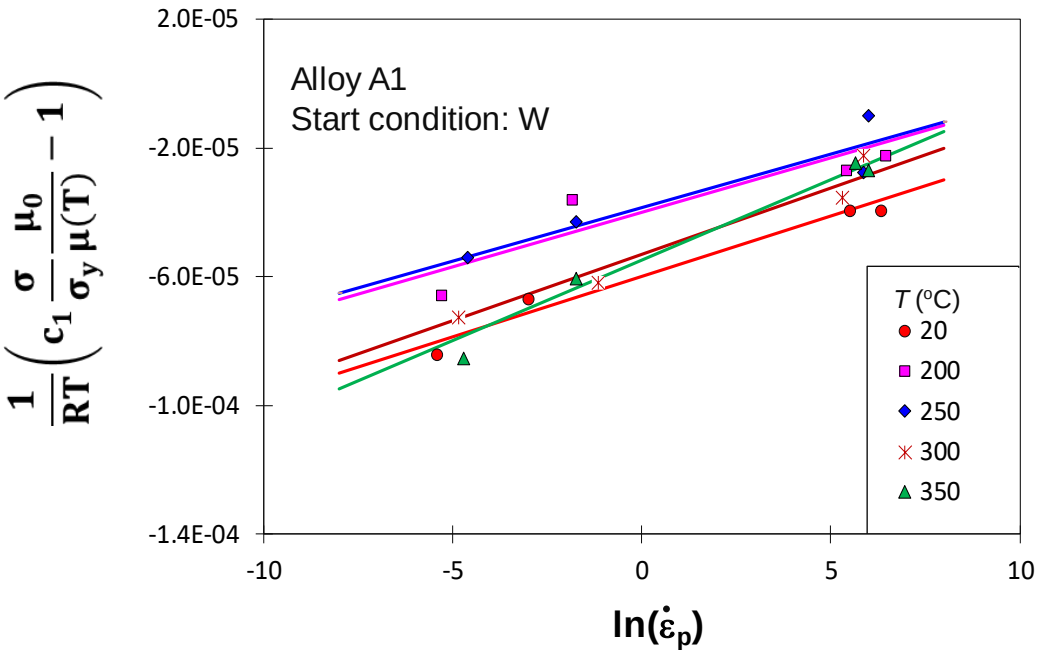

Fig. 5. Diagram used to estimate the activation energy ΔG of cutting or bypassing of barriers in the expression for obstacle limited dislocation glide. Each line represents the least squares regression line for the measurements related to the specific temperature.

After calibration of ΔG, all the adjustable parameters in Eq. [17] are known and summarized in Table II. This allows calculations of the flow stress as a function of temperature and strain rate for small plastic strains when the work hardening can be ignored. Figure 6 shows a comparison between modelling results and measurements for the same experiments as presented in Figure 5, i.e., alloy A1 subjected to strain rates between 0.01 and 750 s^{-1}, temperatures between 20 and 350^{o}C, and a plastic strain of 0.01. From the figure, it is evident that the agreement between calculations and measurements is good for most of the strain rate and temperature combinations covered by the experiments. It may be surprising to find that the experimental data for 250^{o}C show the worst match with the model, even though the ΔG value for this temperature, as obtained from Figure 5, corresponds almost perfectly with the selected ΔG value of 300 kJ/mol. For this temperature, a higher reference strain rate $\dot{\varepsilon}_0$ than the selected value of 10^6 s^{-1} would have given a better agreement between calculations and measurements.

Even though the measurements in Figure 6 consist of single data points without any associated statistics, the trends seem consistent with respect to both strain rate and temperature. An indication of the expected scatter of the measurements can be seen from the tests at strain rates in the range between 200-700 s^{-1} where pairs of samples were tested under identical conditions to examine the repeatability. Even though the resulting strain rates are not identical for these pairs of experiments, they are sufficiently similar to be compared. The maximum deviation is found for the tests carried out at 250^{o}C, for which the difference in stress between the two samples is 8 MPa.

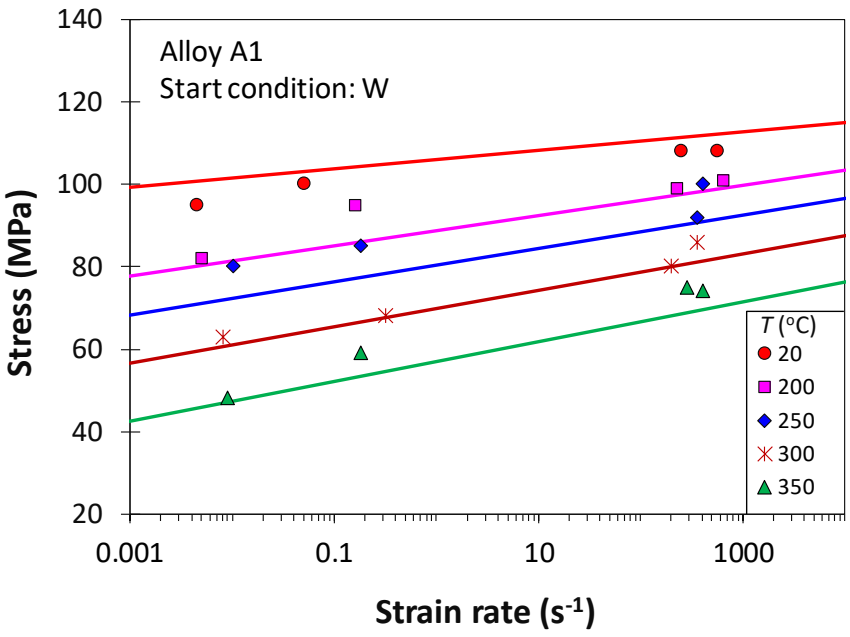

Fig. 6. Stress at a plastic strain of 0.01 (i.e., 1%) as a function of strain rate and temperature. Lines and symbols represent modelling results and measurements, respectively, for alloy A1 in the as-solution heat-treated (W) initial condition.

Including work hardening for a stabile precipitate structure

By increasing the plastic strain, the strength contribution from work hardening, σ_d, cannot be ignored as in the previous section, but must be included in the calculations. Again, alloy A1 is a good alloy for calibration, since the precipitate model described previously predicts that the precipitates can be considered stable during the testing at the different temperatures. This is because the relatively high strain rates used in the experiments give correspondingly short exposure times for the alloy at the elevated temperatures.

Another simplifying assumption for the present calibration using alloy A1 is that only statistically stored dislocations can be assumed to contribute to the observed work hardening behavior. This is because the number density of non-shearable particles is very low in the as-cast and homogenized condition, which in turn leads to a large geometric slip distance λ_g and a correspondingly low ρ_g according to Eq. [14].

Due to the above assumptions, which are related to the precipitate structure of alloy A1, Eq. [16] can be applied in a very simple form corresponding to the well-known Voce equation, since the second term inside the square root, expressing ρ_g, can

be ignored. The only unknown parameters needed to calculate σ_d in Eq. [16], are therefore the parameters related to the dynamic recovery constant k_2 as expressed by Eq. [12]. These parameters are k_2^0, Z_s and m, where the value for the latter parameter has been set to 1/3, in agreement with the original Bergstrøm model [29]. The value for k_2^0 is estimated to 18.0 from Reference 32.

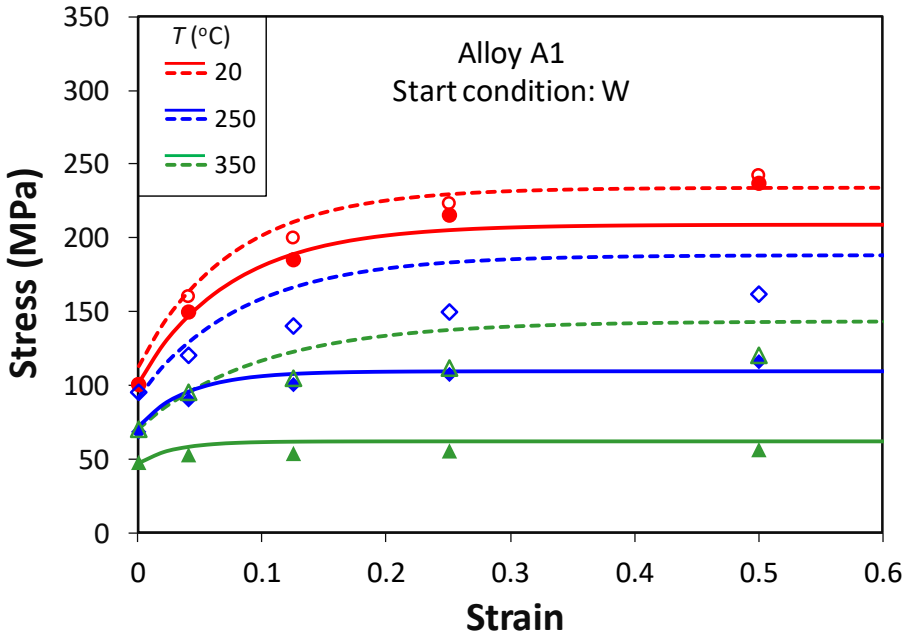

Fig. 7. Comparison between measured and calculated stress-strain curves for alloy A1 in the initial W-condition for three different temperatures, i.e., 20, 250 and 350°C, and two different strain rates, i.e., 0.01 s^{-1} and 750 s^{-1}. Solid lines and filled symbols represent calculations and measurements, respectively, for a strain rate 0.01 s^{-1}. Broken lines and open symbols represent calculations and measurements, respectively, for a strain rate of 750 s^{-1}.

The remaining unknown parameter Z_s in Eq. [12] was determined as the best fit value for the calculated stress-strain curves in Figure 7 when they were compared with the measured data. The best fit value was $Z_s = 1.0 \times 10^5\ s^{-1}$. Figure 7 shows a comparison between measured and calculated stress-strain curves for alloy A1 for three different temperatures, i.e., 20, 250 and 350°C, and the two extreme strain rates used in the experiments, i.e., 0.01 and 750 s^{-1}, respectively. A closer inspection of the figure

reveals that the agreement between calculations and measurements is good, and that the work hardening is reasonably well captured by the model even though there are some deviations. Some of the deviations can probably be ascribed to the fact that the model ignores stage IV work hardening, which is expected to give inaccurate modelling results at large strains.

B. *Dynamic evolution of the precipitate structure during plastic straining*

Until now, it has been assumed that the precipitate structure remains unchanged during the plastic straining. With increasing temperature and decreasing strain rate, this assumption will eventually be violated, and the precipitate structure will change significantly during the straining. The modelling then becomes more complicated than for a stable precipitate structure. A solution algorithm is then required where the evolution of the precipitate structure must be calculated for each time step, and the instantaneous precipitation parameters must be transferred to the yield stress and work hardening model as illustrated in Figure 1.

No work hardening

Also in situations where the precipitate structure evolves during the deformation, it is less complicated to consider small plastic strains first when the work hardening can be ignored. This is done in Figure 8, which shows the flow stress for a plastic strain of 0.001 (i.e., 0.1%) for alloy A3 as a function of the deformation temperature. The different curves and symbols in the figure represent three different strain rates, i.e., 10^{-3}, 10^{-4} and 10^{-5} s^{-1}. The simulation results presented in the figure were carried out by first predicting the precipitate structure for the alloy after the initial T6 heat treatment as specified previously in the experimental section. The predicted precipitate structure in the T6-condition was used as a starting point for the simulations of the evolution of the precipitate structure during the period of plastic straining at various temperatures. The total holding time at each temperature corresponds to $0.001/\dot{\varepsilon}_p$, i.e., 1, 10 and 100 seconds for strain rates of 10^{-3}, 10^{-4} and 10^{-5} s^{-1}, respectively, which were the strain rates used in the tests. Figure 8(a) shows the calculated flow stress σ as a function of the deformation temperature for each of the three strain rates. In these simulations, σ was calculated from Eq. [17] based on the room-temperature yield stress σ_y that the model predicts for the precipitate structure at

681 the end of each deformation, and by using Eq. [19] to convert σ_y to $\hat{\sigma}$. As expected, the
682 calculated stress decreases with increasing temperature and decreasing strain rate,
683 which follows directly from Eq. [17]. The figure also shows the results of the
684 calculations when assuming that the precipitate structure remains unchanged until the
685 end of the deformation. It is evident that this assumption does not affect the results at
686 low temperatures where the reactions are too slow to give any significant change of the
687 precipitate structure. However, the inaccuracy resulting from the simplified assumption
688 of a stable precipitate structure becomes gradually more severe with increasing
689 temperatures above about 230°C, as shown by the difference between the broken and
690 solid lines in the figure.

691

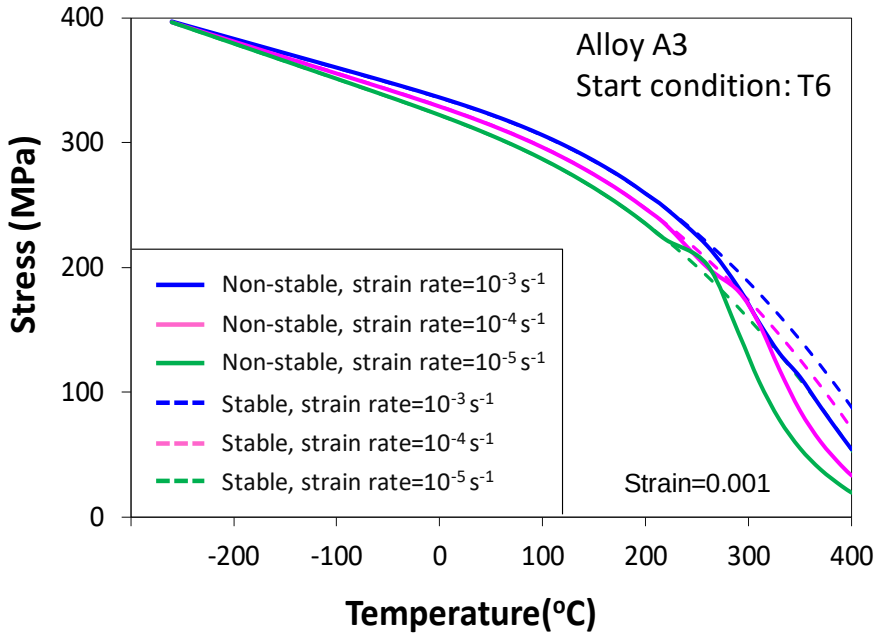

692

693

694 (a)

695

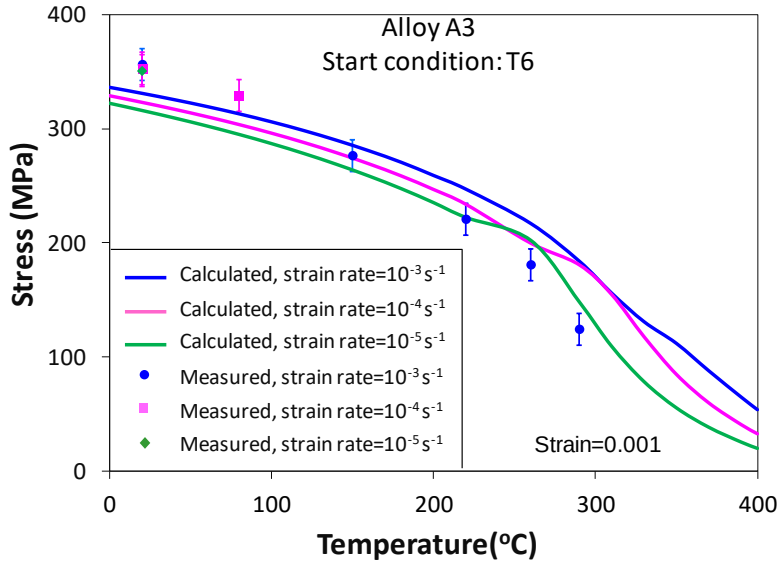

(b)

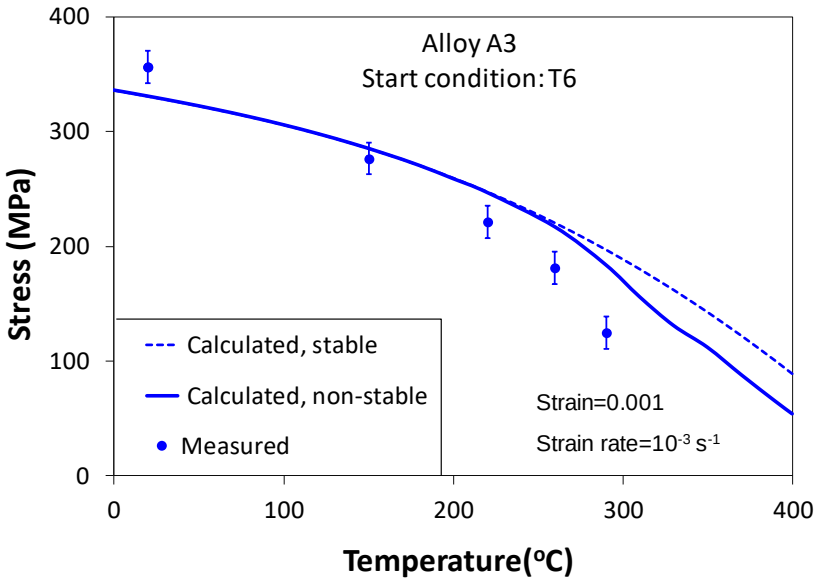

(c)

Fig. 8. Stress at 0.001 (i.e., 0.1%) strain as a function of temperature for alloy A3 in the initial T6-condition. (a) Calculated curves for three different strain rates, i.e., 10^{-3} s^{-1}, 10^{-4} s^{-1}, and 10^{-5} s^{-1}. (b) Comparison between calculations and measurements for the three strain rates. Note that the temperature axis is not the same as in (a). (c) Comparison between calculated stresses based on a stable and a non-stable precipitate structure, respectively, and corresponding measurements. The error bars correspond to ±1 SD, and are based on four parallel tests at room temperature with a strain rate of 10^{-4} s^{-1}.

Figure 8(b) shows a comparison between modelling results and measurements. Despite some deviations, it is evident that the model captures the main trends of the experiments. As shown in Figure 8(c), it is also obvious that the more complex solution, which accounts for the evolution of the precipitate structure during the deformation, gives better agreement with the test results than the simplified solution assuming a stable precipitate structure.

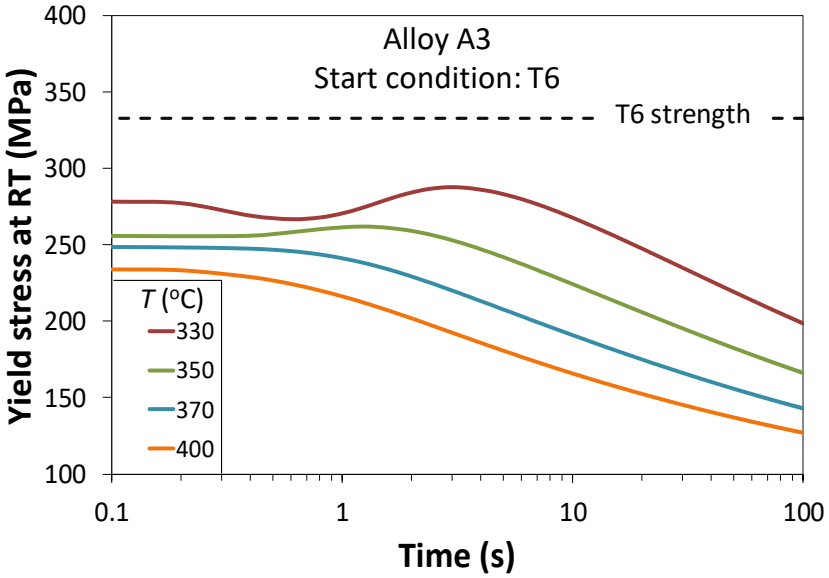

Fig. 9. Model results for the room-temperature yield stress evolution as a function of exposure time at the deformation temperature for alloy A3 in the initial T6-condition. The time axis starts at the end of the heating cycle, i.e., the heating time is excluded.

The predicted curves in Figure 8 show a complex shape above the temperature where the precipitate structure becomes non-stable during the time it takes to conduct the tensile tests. For example, the curve for the strain rate of 10^{-4} s^{-1}, which is located in between the two curves representing 10^{-5} and 10^{-3} s^{-1} at low temperatures, intercept both these curves at temperatures above 230°C as can be clearly seen in Figure 8(b). The reason for this intricate material response can be understood when considering the evolution of the room-temperature yield stress σ_y defined in Eq. [1] during the exposure time at different temperatures. This is shown in Figure 9, where the evolution of σ_y is plotted as a function of the holding time at different temperatures. Here, the initial

values of σ_y are lower than the indicated T6 strength. This is because the precipitate structure evolves during the heating, resulting in a lower σ_y than the T6 strength when the deformation temperature is approached. Some of the curves, like the one for $T = 330$℃, show a complex behavior, where σ_y varies from periods with decreasing to periods with increasing values, which is due to corresponding variation predicted by the precipitate model. It is obvious that this variation of σ_y can explain the interception of the curves with different strain rates shown in Figures 8(a) and 8(b). This is because the different strain rates associated with each curve are directly related to the time axis in Figure 9 through the relationship $t = \varepsilon_p/\dot{\varepsilon}_p$.

Including work hardening for a non-stable precipitate structure

Finally, the most complex situation is considered, i.e., an alloy where the precipitate structure evolves during the plastic deformation at the same time as the plastic strain is large enough to give a significant work hardening. The results from such simulations are compared with measurements for alloy A2 in Figure 10. The simulation results in this figure are based on two different initial precipitate structures, corresponding to the as-solution heat treated (W) and the peak aged (T6) conditions. In the W-condition, the simulations started with cooling from the solid solution temperature, which was the starting point for the following simulations at the different deformation temperatures. For the T6-condition, the simulations started as for the W-condition, but included heating to the artificial ageing temperature of 170^{o}C, and holding at this temperature until NaMo predicted a peak in the yield strength. The precipitate structure for the predicted T6-strength was the starting point for the subsequent simulations of the tensile behavior at different temperatures and strain rates.

Figure 10(a) shows a comparison between predicted and measured tensile curves at 20^{o}C for the initial T6- and W-conditions, respectively. In the simulations, a sudden jump in the strain rate from 0.001 to 0.01 s^{-1} is imposed at a strain of approximately 0.04. The effect of this strain rate increase is not possible to distinguish neither in the experimental data nor in the modelling results for the 20^{o}C case. This is different when testing at higher temperatures for the initial T6-condition, where both measurements and predictions show a pronounced increase of the imposed stress at the onset of the strain rate jump, as is evident from Figures 10(b), 10(c) and 10(d). For the W-condition, the effect of a sudden increase in the strain rate is significantly smaller

761 than for the T6-condition, and the effect can hardly be seen except for the curves in
762 Figure 10(d) corresponding to 340°C. The reason for this difference between the T6-
763 and W-conditions with respect to the jump in strain rate, is the difference in the dynamic
764 recovery response between these two conditions, as will be further discussed below.

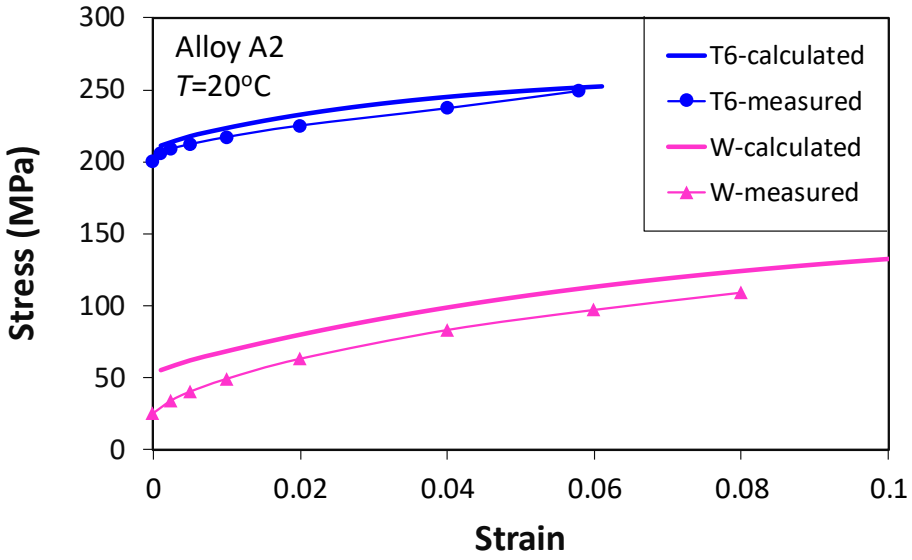

765

766 (a)

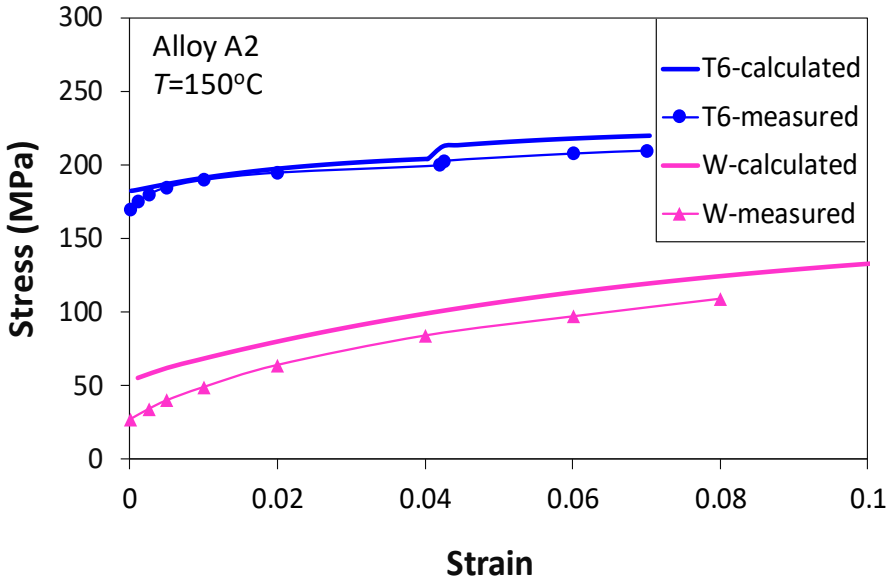

767

768 (b)

769

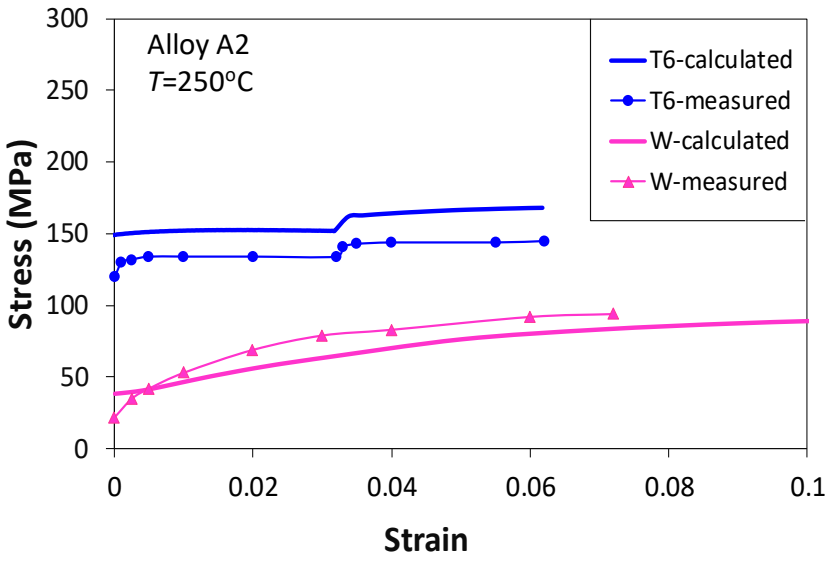

(c)

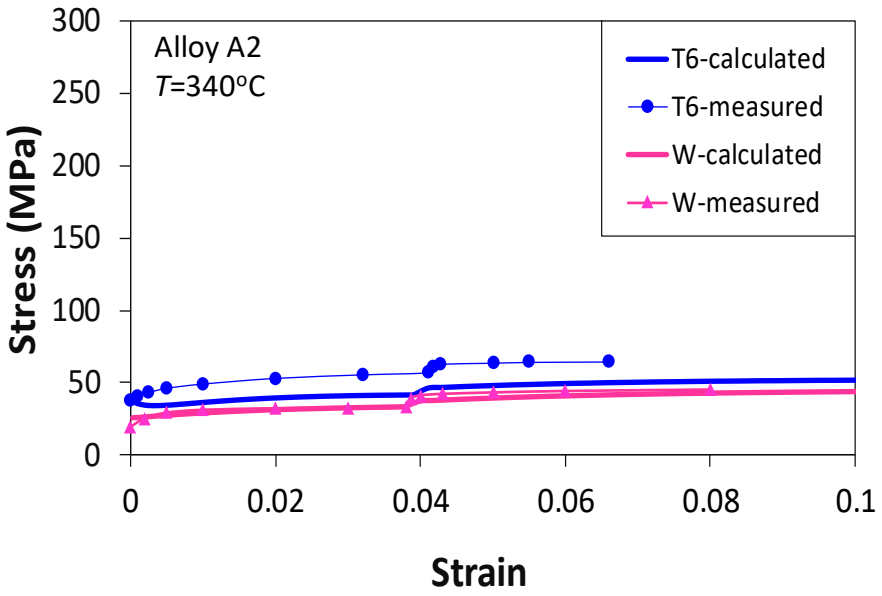

(d)

Fig. 10. Comparison between measured and calculated stress-strain curves for alloy A2 in two different initial conditions, i.e., as-solution heat treated (W) and peak aged (T6). The strain rate is initially 0.001 s^{-1} but increases abruptly to 0.01 s^{-1} at a certain strain, which corresponds to the sudden stress increase in the graphs. The temperatures are: (a) 20°C, (b) 150°C, (c) 250°C, and (d) 340°C.

Even though there are some deviations, the overall agreement between simulation results and measurements in Figure 10 is reasonable. This is particularly the

782 case when taking into consideration that no tuning of the input parameters has been
783 done, as the only inputs to the simulations are the chemical composition and the
784 thermomechanical processing history.

785 The deviations between model simulations and measurements that are observed
786 for some of the stress-strain curves in Figure 10, are most likely due to inaccurate
787 predictions by the precipitation model. Even though the precipitation model usually
788 gives quite accurate predictions [20,35], it is demanding to predict the precipitate structure
789 after an ageing heat treatment followed by reheating to a specific temperature as has
790 been done in the model simulations in Figure 10. It is obvious that the accuracy of the
791 predicted stress-strain curves depends critically on the outputs from the precipitation
792 model. A under- or overestimation of the predicted particle number density will for
793 example lead to a corresponding under- or overestimation of the yield stress.

794 For some of the results presented in Figure 10, the precipitate structure remains
795 unchanged during the tensile test. Still, it is not possible to use the analytical solution
796 presented above to calculate the resulting strain, since the contribution from work
797 hardening cannot be calculated from Eq. [16] when the strain rate or the temperature
798 varies during the tensile test.

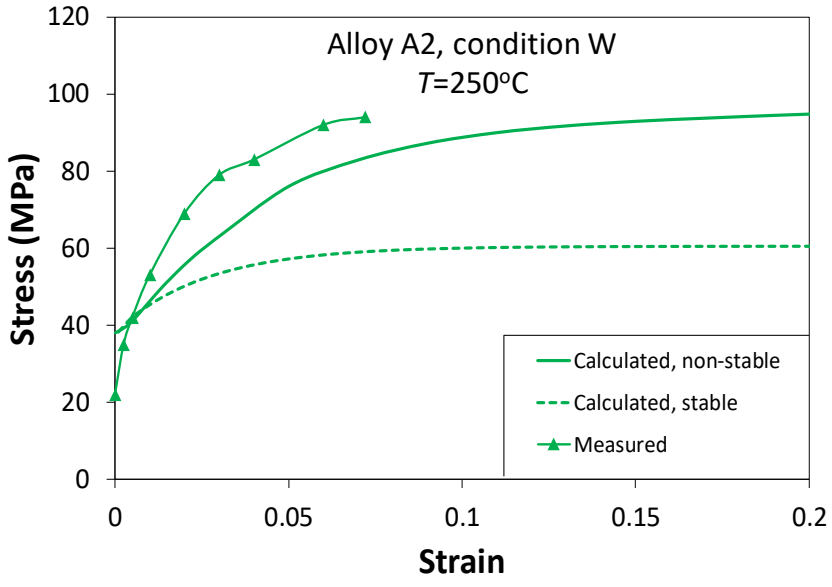

799

800 (a)

801

802

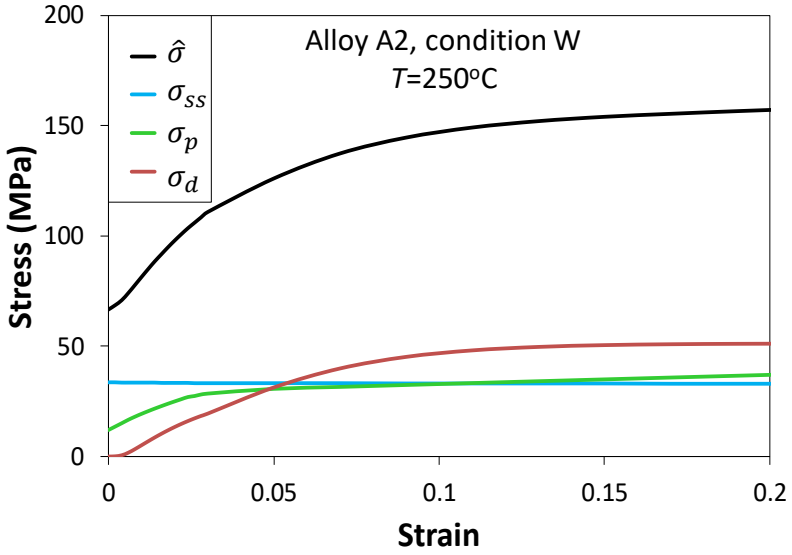

(b)

Fig. 11. (a) Comparison between calculated stress-strain curves based on a stable and a non-stable precipitate structure, respectively, and corresponding measurements. (b) Evolution of the room-temperature yield stress contributions σ_{ss}, σ_p, and σ_d as well as the equivalent overall yield stress at 0 K, i.e., $\hat{\sigma}$ during the plastic deformation. The alloy and temper conditions in (a) and (b) correspond to the one shown in Figure 10(c).

An example of the possible error that can be introduced by assuming a constant precipitate structure when the structure evolves during the tensile test is shown in Figure 11(a). The example is the same as shown previously for the initial W-condition in Figure 10(c), but in Figure 11(a) an additional calculation has been carried out using the simplified solution expressed by Eq. [16] to calculate σ_d. In the simplified calculation, σ_p and σ_{ss} in Eq. [1] are assumed to remain constant with their initial values throughout the tensile test. It is evident from Figure 11(a) that the error introduced by this simplification is severe since the predicted stress is 59MPa for the simplified solution at a strain of 0.07, compared to a measured value of 93MPa. The corresponding yield stress when accounting for the evolution of the precipitate structure is 83MPa, which is a significantly better estimate. Figure 11(b) shows how the different contributions to the room-temperature yield stress evolves as a function of the plastic strain. A closer inspection of the figure reveals that σ_p increases from 0 to 40 MPa when

824 the plastic strain increases from 0 to 0.07. This strength increase is disregarded in the
825 simplified solution that assumes that the precipitate structure is unchanged from start to
826 the end of the tensile test. Hence, it is evident that in the present case, the severe
827 underestimation of the applied stress that the simplified solution provides is mainly
828 caused by ignoring σ_p.

829 Finally, an example of predictions of the evolution of the dislocation density
830 during tensile testing is shown in Figure 12. The predictions are based on the test
831 presented in Figure 10(c) where alloy A2 was subjected to an imposed tensile loading
832 at 250°C with an initial strain rate of 0.001 s^{-1}. The figure shows the gradual increase in
833 the densities of geometrically necessary dislocations (ρ_g) and statistically stored
834 dislocations (ρ_s) when the strain increases. The initial conditions are T6 and W in
835 Figures 12(a) and 12(b), respectively.

836

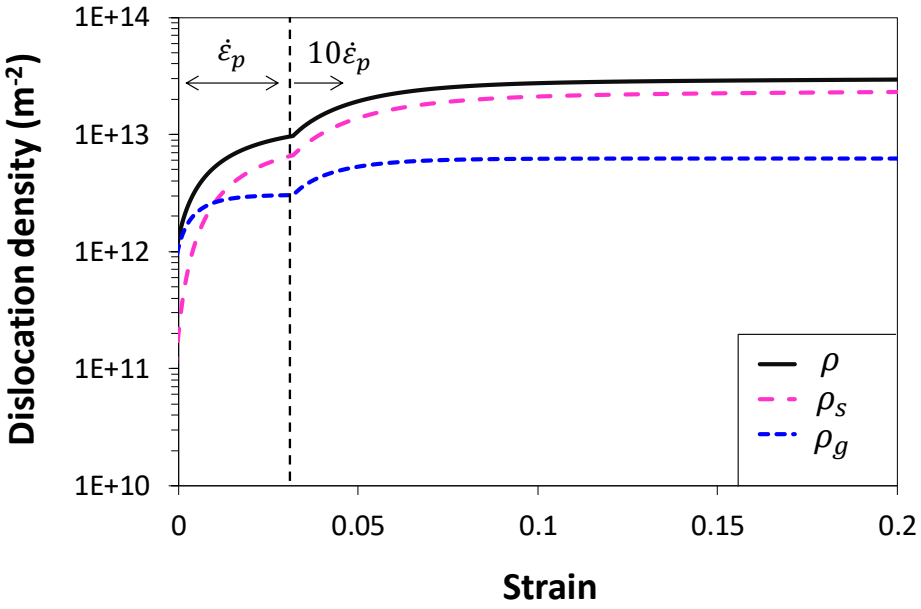

837

838 (a)

839

840

841

842

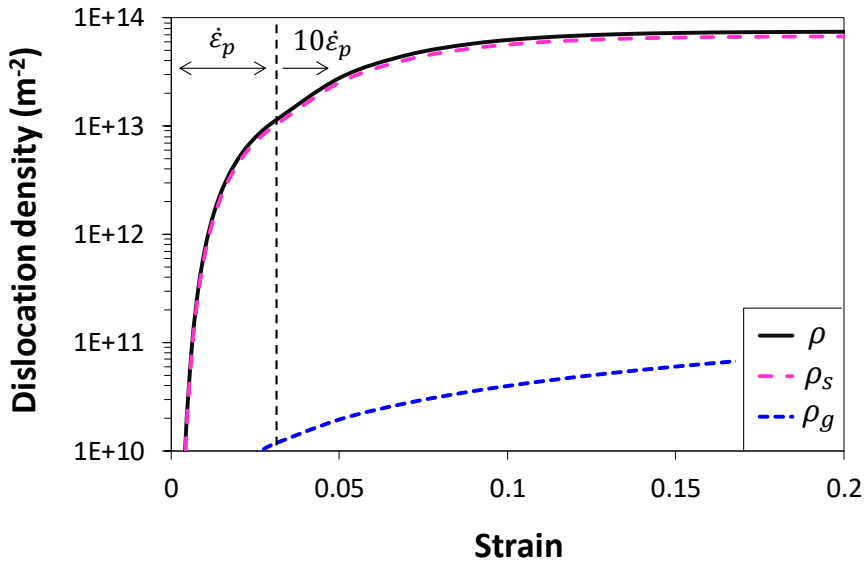

(b)

Fig. 12. Evolution of geometrically necessary dislocation density (ρ_g), statistically stored dislocation density (ρ_s) and total dislocation density (ρ) during tensile testing of alloy A2 at 250°C. The strain rate is suddenly increased from 0.001s^{-1} to 0.01s^{-1} at a strain of 0.03 as indicated in the figure. (a) Initial T6-condition. (b) Initial W-condition.

The dislocation density curves are clearly different in Figures 12(a) and 12(b). In Figure 12(a), ρ_g dominates at small plastic strains due to the presence of a relatively large volume fraction of non-shearable particles in the initial T6-condition. At larger strains, ρ_s dominates. The interception of the two curves is closely related to the slip distances λ_g and $1/\sqrt{\rho_s}$ for geometrically necessary and statistically stored dislocations, respectively. λ_g may increase or decrease during the plastic straining, while $1/\sqrt{\rho_s}$ usually decreases with increasing plastic strain. This may lead to a shift from a plastic strain region characterized by the presence of predominantly geometrically necessary dislocations to a region with mainly statistically stored dislocations, which is typical for alloys containing non-shearable particles [47]. Figure 12(b) shows corresponding dislocation density-strain curves for the same alloy in the initial W-condition. The most evident difference from the curves in Figure 12(a) is that

statistically stored dislocations dominates over the whole range of plastic strains. This is due to a low volume fraction of non-shearable particles in the as-solution heat treated W-condition.

The results in Figure 12 also illustrates the effect of a jump in the strain rate during the tensile test. As indicated in the figures, the plastic strain rate was suddenly increased by a factor 10 to $0.01s^{-1}$ at a strain of 0.03. For the alloy in the initial T6-condition in Figure 12(a), this jump in strain rate is clearly reflected in the simulation results, which show a corresponding sudden increase in the slopes of the curves at this critical strain. The reason for the rapid increase in the storing rate of dislocations when the strain rate is increased, is a corresponding shortening of the time available for dynamic recovery, as expressed by k_2 and k_{2g} in Eqs. [12] and [15], respectively.

For the initial W-condition shown in Figure 12(b), no pronounced change in the slope of the dislocation density curves can be observed at the transition between slow and fast strain rate, which is consistent with the measured tensile curves in Figure 10(c). The reason why the W-condition is insensitive to the abrupt increase in strain rate, is a relatively weak influence of the strain rate on k_2 and k_{2g} for this specific combination of particle structure and solid solution concentrations as calculated by the precipitation model.

C. *Accuracy of the simulations*

Overall agreement between simulation results and measurements

In order to quantify the predictive power of the new version of the NaMo model presented in this work, a statistical analysis was performed where the relative deviation between predicted and measured values was calculated for all alloys and testing conditions. The results are shown in Figure 13, from which it is evident that the stress data tend to spread evenly on each side of the 45-degree line defining the expected (mean) values in the plot. Assuming that the observed spread of the data is normally distributed around this mean, a 68% confidence interval of ±17.3% is obtained for the entire population (equal to ±1 SD).

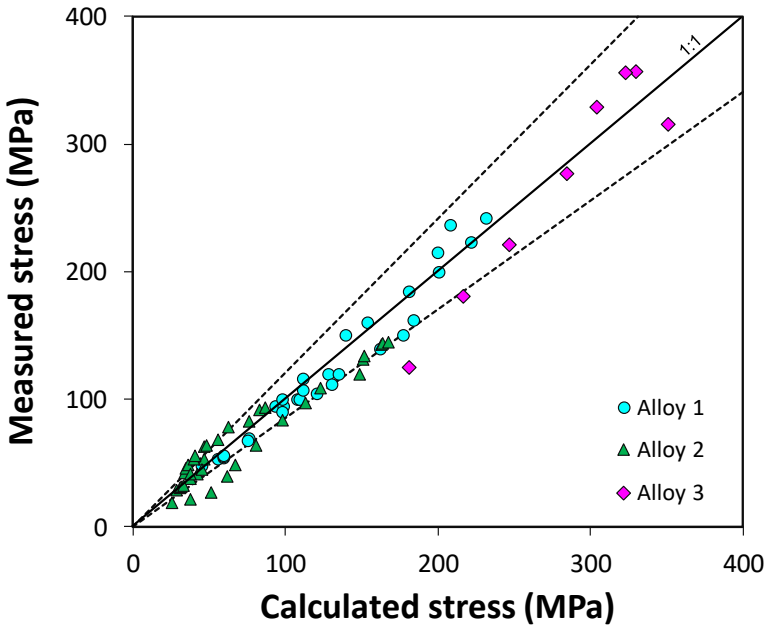

Fig. 13. Evaluation of the predictive power of NaMo, based on a statistical analysis of all test results pertaining to Alloys 1, 2 and 3 (see Table III and IV for details). In this scatter plot, the broken lines represent the 68% confidence interval.

Adjustable parameters used in the model

In the new NaMo version, several parameters have been introduced related to the models for obstacle limited dislocation glide and work hardening. For the former model, some evaluations of the reliability of the chosen values for c_1, ΔG, $\dot{\varepsilon}_0$, p and q were given in previous sections, without any detailed quantitative analysis on the combined effect of these parameters on the resulting flow stress, which is beyond the scope of the present work.

For the modified work hardening model, the parameters that have been introduced are related to dynamic recovery of statistically stored and geometrically necessary dislocations as given by Equations [12] and [15], respectively. The corresponding parameters that have been calibrated are Z_s and Z_g in Equation [12] and [15], respectively. The former parameter is deemed quite accurate since there are several experimental stress-strain curves available for alloy A1 that are relevant for its calibration. This is in contrast to the estimated Z_g-value, which is associated with more uncertainty since only a few of the experimental stress-strain curves in the present study

are relevant for calibration of this parameter. This is because calibration of Z_g requires materials with a significant amount of large non-shearable particles that form geometrically necessary dislocations during tensile testing. The precipitation model predicts that only a few of the materials in the present study contain substantial amounts of large non-shearable particles at the start of the tensile testing.

Since the Z_g value is more uncertain than the corresponding Z_s value, this means that the calculated curves for geometrically necessary dislocations in Figure 12 are expected to be more uncertain than the corresponding curves for statistically stored dislocations in the same figure.

VI. CONCLUSIONS

The main conclusions that can be drawn from this investigation are as follows:

1. A framework for modelling the relationship between stress, strain, strain rate and temperature in age hardening Al-Mg-Si alloys has been presented. It is shown that the stability of the precipitate structure must be given due attention in the analysis, and that analytical solutions can be used if the precipitate structure remains essentially unchanged during the plastic deformation.
2. In the article, the boundaries between stable and non-stable precipitate structures have been derived for two different initial conditions, i.e., peak aged (T6) and as-solution heat treated (W).
3. If the precipitate structure changes during the plastic straining, the numerical model (NaMo) outlined in the present article, is required with a full coupling between precipitation, yield strength and work hardening calculations for each time step of the simulation.
4. The predictive capability of the model is good, as verified by comparisons between simulation results and measurements for three different alloys subjected to temperatures between 20 and 350^{o}C, and strain rates ranging from 10^{-6} to 750 s^{-1}.
5. Finally, it is concluded that the combined precipitation, yield strength and work hardening model outlined above provides a powerful tool for different industrial problems ranging from predictions of thermal stability and creep behavior of alloys, to energy absorption at high strain rates at various temperatures.

VII. FUTURE WORK

The new version of the NaMo model presented in the present study represents a complete thermomechanical simulation model for Al-Mg-Si alloys. From the comparison between simulation results and measurements in present and previous works, it seems like the precipitation model represents the most critical part when it comes to accuracy of the simulations. This is not surprising considering the complexity of the precipitation sequence in this type of alloys, with interactions between several metastable phases, dislocation structures and vacancies. Hence, a main goal for future work will be to develop further the precipitation model by including multi-component thermodynamic databases and to improve the handling of vacancies and their effect on the precipitation kinetics. The NaMo model has already been implemented as an industrial tool in alloy development and processing of 6xxx series aluminum alloys. Furthermore, work is in progress to implement the model in general-purpose finite element codes for simulations of the mechanical response during various loading situations including impact and crash of structural members like automotive components and parts.

ACKNOWLEDGMENTS

The authors gratefully appreciate the financial support from NTNU and the Research Council of Norway through the FRINATEK Program, Project No. 250553 (FractAl), and the Centre for Advanced Structural Analysis, Project No. 237885 (CASA).

APPENDIX

Symbols and units

b	magnitude of the Burgers vector (m)
C_i	concentration of specific element *i* in expression for σ_{ss} (wt%)
C_{ss}	equivalent solid solution concentration (wt%)
C_{ss}^r	value of C_{ss} for reference alloy (wt%)
c_1	conversion factor for yield stress from 0K to room temperature.
$\bar{F}$	mean interaction force between particle and dislocation (N)
f	particle volume fraction
f_o	volume fraction of non-shearable Orowan particles
f_o^r	value fraction of f_o in reference alloy
k_i	scaling factor in expression for σ_{ss} (MPa/(wt%)$^{2/3}$)
k_1	parameter related to statistical storage of dislocations (m^{-1})
k_{1g}	parameter related to statistical storage of geometrically necessary dislocations (m^{-1})
k_2	parameter related to dynamic recovery of dislocations
k_{2g}^0	constant in expression for k_{2g}
k_{2g}	parameter related to dynamic recovery of geometrically necessary dislocations
k_2^0	constant in expression for k_2
k_2^*	constant in expression for dynamic recovery of dislocations
k_2^r	value of k_2 in reference alloy
k_3	parameter determining the solute dependence of k_2 (N/m^{2}wt%$^{3/4}$)
l	mean planar particle spacing along the bending dislocation (m)
M	Taylor factor

995	M_r	Taylor factor for reference alloy
996	m	constant in expression for dynamic recovery of dislocations
997	N_i	number of particles per unit volume within the size class r_i (#/m^3)
998	p	constant in expression for σ
999	q	constant in expression for σ
1000	Q_d	activation energy for diffusion (J/mol)
1001	R	universal gas constant (8.314 J/Kmol)
1002	r	particle radius (m)
1003	r_i	particle radius within size class *i* (m)
1004	r_c	critical particle radius for the transition from shearing to bypassing (m)
1005	t	time (s)
1006	T	temperature (K or ^{o}C)
1007	T_m	melting temperature (K or ^{o}C)
1008	T_r	room temperature (K or ^{o}C)
1009	Z	Zener-Hollomon parameter (s^{-1})
1010	Z_0	Zener-Hollomon parameter at 0 K (s^{-1})
1011	Z_r	Zener-Hollomon parameter for reference alloy (s^{-1})
1012	Z_s	constant in expression for k_2 (s^{-1})
1013	Z_g	constant in expression for k_{2g} (s^{-1})
1014	α	constant in expression for σ_d
1015	ΔG	activation energy required to overcome obstacles without aid from
1016		external stresses (J/mol)
1017	ε	tensile strain
1018	$\dot{\varepsilon}$	tensile strain rate (s^{-1})
1019	$\dot{\varepsilon}_0$	reference strain rate in expression for σ (s^{-1})

1020	$\dot{\varepsilon}_r$	strain rate for reference alloy (s^{-1})
1021	ε_p	plastic tensile strain
1022	θ_g	material constant in expression for the temperature dependence of μ
1023	λ_g	geometric slip distance (m)
1024	μ	shear modulus (N/m^2)
1025	μ_r	shear modulus for reference alloy (N/m^2)
1026	μ_0	shear modulus at 0 K (N/m^2)
1027	ρ_g	number density of geometrically necessary dislocations (m^{-2})
1028	ρ_s	number density of the statistically stored dislocations (m^{-2})
1029	σ	flow stress (N/m^2)
1030	$\hat{\sigma}$	yield stress at 0 K (N/m^2)
1031	σ_d	net contribution from dislocation hardening to flow stress (N/m^2)
1032	σ_i	intrinsic yield strength of pure aluminum (N/m^2)
1033	σ_p	contribution from hardening precipitates to the overall macroscopic
1034		yield strength (N/m^2)
1035	σ_{p1}	contribution from clusters to the overall macroscopic yield strength
1036		(N/m^2)
1037	σ_{p2}	contribution from hardening β'' and β' to the overall macroscopic yield
1038		strength (N/m^2)
1039	σ_{ss}	contribution from alloying elements in solid solution to the overall
1040		macroscopic yield strength (N/m^2)
1041	σ_y	overall macroscopic yield strength (N/m^2)
1042		

REFERENCES

1. G. Edwards, K. Stiller, G. Dunlop, and M. Couper: *Acta Mater.*, 1998, vol. 46, pp. 3893-04.
2. M. Murayama, K. Hono, M. Saga, and M. Kikuchi: *Mater. Sci. Eng. A*, 1998, vol. 250, pp. 127-32.
3. I. Dutta, and S.M. Allen: *J. Mater. Sci. Lett.*, 1991, vol. 10, pp. 323-26.
4. W.F. Miao and D.E. Laughlin: *Scripta Mater.*, 1999, vol. 40, pp. 873-78.
5. C.D. Marioara, S.J. Andersen, J. Jansen, and H.W. Zandbergen: *Acta Mater.*, 2001, vol. 49, pp. 321–28.
6. J.S. Langer and A.J. Schwartz: *Physical Review A, The American Physical Society*, 1980, vol. 21, pp. 948-958.
7. R. Kampmann, H. Eckerlebe, and R. Wagner: *Mat. Res. Soc. Symp. Proc.*, MRS, 1987, vol. 57, pp. 525-42.
8. R. Wagner and R. Kampmann: *Material Science and Technology - A Comprehensive Treatment*, vol. 5, VCH, 1991, pp. 213-03.
9. A. Bahrami, A. Miroux, and J. Sietsma: *Metall. Mater. Trans. A*, 2012, vol. 43A, pp. 4445-53.
10. D. Bardel, M. Perez, D. Nelias, A. Deschamps, C. R. Hutchinson, D. Maisonnette, T. Chaise, J. Gamier, and F. Bourlier: *Acta Mater.*, 2014, vol. 62, pp. 129-140.
11. Q. Du, B. Holmedal, J. Friis, and C. Marioara: *Metall. Mater. Trans. A*, 2016, vol. 47A, pp. 589-599.
12. Q. Du, K. Tang, C.D. Marioara, S.J. Andersen, B. Holmedal, and R. Holmestad: *Acta Mater.*, 2017, vol. 122, pp. 178-186.
13. M. Perez, M. Dumont, and D. Acevedo-Reyes: *Acta Mater.*, 2008, vol. 56, pp. 2119-32.
14. Q. Du, Y. Li: *Acta Mater.* 2014, vol. 71, pp. 380-389.

15. P. Maugis P, M. Goune: Acta Mater. 2005, vol. 53, pp. 3359-67.

16. Q. Du, W.J. Poole, M.A. Wells: *Acta Mater.*, 2012, vol. 60, pp. 3830-39.

17. Q. Chen, J. Jeppsson, J. Ågren: *Acta Mater.*, 2008, vol. 56, pp. 1890-96.

18. E. Kozeschnik, I. Holzer, B. Sonderegger: *J. Phase Equilibria Diffusion*, 2007, vol. 28, pp. 64-71.

19. A. Deschamps and Y. Bréchet: *Acta Mater*. 1999, vol. 47, pp. 293-305.

20. O.R. Myhr, Ø. Grong, and S.J. Andersen: *Acta Mater.*, 2001, vol. 49, pp. 65-75.

21. L.M Cheng, W.J. Poole, J.D. Embury, and D.J. Lloyd: *Metall. Mater. Trans. A*, 2003, vol. 34A, pp. 2473-81.

22. W.J. Poole and D.J. Lloyd: *Proc. 9th Int. Conf. on Aluminium Alloys*, Institute of Materials Engineering Australasia Ltd, 2004, pp. 939-44.

23. U.F. Kocks: *J. Eng. Mater. Technol.*, 1976, vol. 98, pp. 76-85.

24. H. Mecking and U.F. Kocks: *Acta Metall.*, 1981, vol. 29, pp. 1865-75.

25. Y. Estrin: in *Unified Constitutive Laws of Plastic Deformation*, A.S. Krausz and K. Krausz, eds., Academic Press, New York, NY, 1996, pp. 69-106.

26. Y. Estrin: J. of Mater. Proc. Technol., 1998, vols. 80-81, pp. 33-39.

27. H. J. Frost, and M. F. Ashby: *Deformation-Mechanism Maps. The Plasticity and Creep of Metals and Ceramics*, Oxford (England), Pergamon Press, 1982.

28. A.G. Evans and R.D. Rawlings: *Phys. Stat. Sol.*, 1969, vol. 34, pp. 9-31.

29. Y. Bergström, H. Hallén*: Mater. Sci. Eng.*, 1982, vol. 55, pp. 49-61.

30. A.H. van den Boogaard and J. Huétink: *Comput. Methods Appl. Mech. Engrg.*, 2006, vol. 195, pp. 6691-6709.

31. O.R. Myhr, Ø. Grong and C. Schäfer: *Metall. Mater. Trans A*, 2015, vol. 46A, pp. 6018-39.

32. O.R. Myhr, Ø. Grong, and K.O. Pedersen: *Metall. Mater. Trans. A*, 2010, vol. 41A, pp. 2276-89.

33. O.R. Myhr, and Ø. Grong: *Acta Mater.*, 2000, vol. 48, pp. 1605-15.

34. O.R. Myhr, and Ø. Grong: *ASM Handbook, Welding Fundamentals and Processes*, ASM, vol. 6A, 2011, pp. 797-18.

35. O.R. Myhr, Ø. Grong, H.G. Fjær and C.D. Marioara: *Acta Mater.*, 2004, vol. 52, pp. 4997-08.

36. J.K. Holmen, T. Børvik, O.R. Myhr, H.G. Fjær, O.S. Hopperstad: *International Journal of Impact Engineering*, 2015, vol. 84, pp. 96-107.

37. J. Johnsen, J.K. Holmen, O.R. Myhr, O.S. Hopperstad, T. Børvik: *Comp. Mat. S.*, 2013, vol. 79, pp. 724-735.

38. C. Dørum, O.G. Lademo, O.R. Myhr, T. Berstad, O.S. Hopperstad: *Computers & Structures*, 2010, vol. 88, pp. 519–528.

39. A.J.E. Foreman and M.J. Makin: *Phil. Mag.*, 1966, vol. 14, pp. 911-924.

40. L.M. Brown and R.K. Ham: in *Strengthening Methods in Crystals.* A. Kelly and R.B. Nicholson, eds., Applied Science Publishers Ltd., Academic Press, London, 1971, pp. 9-135.

41. A.J. Ardell: *Metall. Mater. Trans. A*, 1985, vol. 61A, pp. 2131-65.

42. U.F. Kocks: *Phil.Mag*., 1966, vol. 13, pp. 541-66.

43. A. Rusinek, J.A. Rodríguez-Martínez: *Materials & Design*, 2009, vol. 30, pp. 4377-90.

44. K. Teichmann, C.D. Marioara, S.J. Andersen, and K. Martinsen: *Metall. Mater. Trans. A*, 2012, vol. 43A, pp. 4006-14.

45. K. Teichmann, C.D. Marioara, S.J. Andersen, and K. Martinsen: *Materials Characterization*, 2013, vol. 75, pp. 1-7.

46. F. Fazeli, C.W. Sinclair, and T. Bastow: *Metall. Mater. Trans. A*, 2008, vol. 39A, pp. 2297-2305.

47. M. F. Ashby, Phil. Mag.: 1970, vol. 21, pp. 399-424.

48. S. Gouttebroze, A. Mo, Ø. Grong, K.O. Pederesen and H.G. Fjær: *Metall. Mater. Trans. A*, 2008, vol. 39A, pp. 522-534.

49. V. Vilamosa, A.H. Clausen, T. Børvik, S.R. Skjervold, O.S. Hopperstad: *Int. Journal of Impact Engineering*, 2015, vol. 86, pp. 223-239.

50. U.F. Kocks, A.S. Argon, and M.F. Ashby: *Thermodynamics and Kinetics of Slip*, Progress in Materials Science, vol.19, Pergamon, Oxford (England), 1975.

51. V. Vilamosa, A.H. Clausen, T. Børvik, B. Holmedal, O.S. Hopperstad: *Materials & Design*, 2016, vol. 103, pp. 391-405.

52. V. Vilamosa, A.H. Clausen, E. Fagerholt, O.S. Hopperstad and T. Børvik: *Strain*, 2014, vol. 50, pp. 223-235.

53. V. Vilamosa: Doctoral Thesis, Norwegian University of Science and Technology, Department of Structural Engineering, Trondheim, 2015.

54. H.G. Fjær, B.I. Bjørneklett, and O.R. Myhr: *Proc. TMS Annual Meeting*, San Francisco, CA, Feb. 2005, TMS, Warrendale, PA, 2005, pp. 95-100.

FIGURE CAPTIONS

Fig. 1. Coupling of the different sub-models in NaMo, and transfer of data between the sub-models. The symbols used in the figure are explained in the Appendix.

Fig. 2. Example of the predictive capability of the precipitation model in NaMo. Figures (a), (b) and (c) show TEM bright field images of microstructures observed in the <100> Al zone axis orientation after artificial ageing and Gleeble simulation [35]. (a) Needle-shaped β'' precipitates which form after a T6 heat treatment corresponding to solution heat treatment at 530°C for 30 minutes followed by water quenching prior to artificial ageing at 185°C for 5 hours. (b) Mixture of coarse rod-shaped β' particles and fine needle-shaped β'' precipitates which form after subsequent thermal cycling to $T_p = 315℃$ (10 seconds holding time). (c) Coarse rod-shaped β' particles which form after subsequent thermal cycling to $T_p = 390℃$ (10 seconds holding time). (d) Comparison between predictions by the precipitation model and measurements of the particle number density (left-hand axis) and the mean particle radius (right-hand axis).

Fig. 3. Calculated boundaries between stable and non-stable precipitate structures for two different initial conditions, i.e., as-solution heat treated (W) and peak aged (T6).

Fig. 4. Overview of applied temperature and holding time for all tests. The location of the symbols in the diagram relative to the superimposed boundaries indicates whether they are performed with a stable (open symbols) or non-stable (filled symbols) precipitate structure. (a) Initially as-solution heat-treated (W) condition. (b) Initially peak aged (T6) condition.

Fig. 5. Diagram used to estimate the activation energy ΔG of cutting or bypassing of barriers in the expression for obstacle limited dislocation glide. Each line represents the least squares regression line for the measurements related to the specific temperature.

Fig. 6. Stress at a plastic strain of 0.01 (i.e., 1%) as a function of strain rate and temperature. Lines and symbols represent modelling results and measurements, respectively, for alloy A1 in the as-solution heat-treated (W) initial condition.

Fig. 7. Comparison between measured and calculated stress-strain curves for alloy A1 in the initial W-condition for three different temperatures, i.e., 20, 250 and 350°C, and two different strain rates, i.e., 0.01 s^{-1} and 750 s^{-1}. Solid lines and filled symbols represent calculations and measurements, respectively, for a strain rate 0.01 s^{-1}. Broken lines and open symbols represent calculations and measurements, respectively, for a strain rate of 750 s^{-1}.

Fig. 8. Stress at 0.001 (i.e., 0.1%) strain as a function of temperature for alloy A3 in the initial T6-condition. (a) Calculated curves for three different strain rates, i.e., 10^{-3} s^{-1}, 10^{-4} s^{-1}, and 10^{-5} s^{-1}. (b) Comparison between calculations and measurements for the three strain rates. Note that the temperature axis is not the same as in (a). (c) Comparison between calculated stresses based on a stable and a non-stable precipitate structure, respectively, and corresponding measurements. The error bars correspond to ±1 SD, and are based on four parallel tests at room temperature with a strain rate of 10^{-4} s^{-1}.

1184

1185 Fig. 9. Model results for the room-temperature yield stress evolution as a function of
1186 exposure time at the deformation temperature for alloy A3 in the initial T6-condition.
1187 The time axis starts at the end of the heating cycle, i.e., the heating time is excluded.

1188

1189 Fig. 10. Comparison between measured and calculated stress-strain curves for alloy A2
1190 in two different initial conditions, i.e., as-solution heat treated (W) and peak aged (T6).
1191 The strain rate is initially 0.001 s^{-1} but increases abruptly to 0.01 s^{-1} at a certain strain,
1192 which corresponds to the sudden stress increase in the graphs. The temperatures are: (a)
1193 20°C, (b) 150°C, (c) 250°C, and (d) 340°C.

1194 Fig. 11. (a) Comparison between calculated stress-strain curves based on a stable and a
1195 non-stable precipitate structure, respectively, and corresponding measurements. (b)
1196 Evolution of the room-temperature yield stress contributions σ_{ss}, σ_p, and σ_d as well as
1197 the equivalent overall yield stress at 0 K, i.e., $\hat{\sigma}$ during the plastic deformation. The
1198 alloy and temper conditions in (a) and (b) correspond to the one shown in Figure 10(c).

1199

1200 Fig. 12. Evolution of geometrically necessary dislocation density (ρ_g), statistically
1201 stored dislocation density (ρ_s) and total dislocation density (ρ) during tensile testing of
1202 alloy A2 at 250°C. The strain rate is suddenly increased from 0.001s^{-1} to 0.01s^{-1} at a
1203 strain of 0.03 as indicated in the figure. (a) Initial T6-condition. (b) Initial W-condition.

1204

Fig. 13. Evaluation of the predictive power of NaMo, based on a statistical analysis of all test results pertaining to Alloys 1, 2 and 3 (see Table III and IV for details). In this scatter plot, the broken lines represent the 68% confidence interval.

TABLES

Table I. Summary of input parameters used in the yield strength and work hardening models.

Parameter	Value	Comments
b (m)	2.84 x 10^{-10}	Magnitude of Burgers vector
C_{ss}^{r}(wt%)	1.0	Chosen reference concentration
f_0^r	0.0109	From Reference 32
k_1 (m^{-1})	4.0 x 10^8	From Reference 32
k_{1g}(m^{-1})	4.0 x 10^8	From Reference 38
k_2^0	18.0	Estimated value based on data from Reference 32
k_{2g}^0	20.0	From Reference 32
k_3 ($N/m^2 wt\%^{3/4}$)	2.0 x 10^8	From Reference 32
M	3.1	Magnitude of Taylor factor for a random texture
m	1/3	From Reference 29
Z_g(s^{-1})	1.0 x 10^8	Calibrated based on data for alloy A2 in initial T6-condition
Z_s (s^{-1})	1.0 x 10^5	Calibrated based on data for alloy A1
α	0.30	From Reference 42
θ_g	2.295	From Reference 53
μ_0 (MPa)	2.71 x 10^4	From Reference 53
σ_i (MPa)	10	From Reference 19

Table II. Summary of adjustable parameter values in the model for obstacle limited dislocation glide.

Parameter	**Value**	**Comments**
c_1	0.83	Calculated from Eq. [20]
p	1	Reasonable value for Al-Mg-Si alloys [51]
q	1	Reasonable value for Al-Mg-Si alloys [51]
T_r (K)	293	Temperature used when calibrating the RT-model
$\dot{\varepsilon_0}$ (s^{-1})	10^6	From Reference 27
$\dot{\varepsilon_r}$ (s^{-1})	10^{-4}	Typical strain rate used in previous experiments to calibrate the RT yield stress model
ΔG (kJ/mol)	300	Calculated using data for alloy A1

Table III. Chemical composition of alloys used for calibration and validation of the model (weight percent).

Alloy	**Si**	**Mg**	**Cu**	**Mn**	**Fe**	**Cr**	**Al**
A1 (6082)	0.76	0.80	0.24	0.56	0.20	0.16	Balance
A2 (6060)	0.44	0.43	0.02	0.03	0.23	0.006	Balance
A3 (6082)	1.28	0.62	0.09	0.49	0.18	0.14	Balance

1250 Table IV. Range in temperatures and strain rates used in the tests.

Alloy	**Initial condition**	***T*** **(ºC)**	$\dot{\varepsilon}$ **(s^{-1})**	**Tests and References**
A1 (6082)	Homogenized	20-350	10^{-2}-1	Tension tests [49,53]
			1-750	Split-Hopkinson Tension Bar System [52,53]
A2 (6060)	W, T6	20-340	10^{-3}-10^{-2}	Gleeble [48,54]
A3 (6082)	W, T6	20-290	10^{-5}-10^{-3}	Gleeble

1251

1252

1253